



Mesoscopic modeling of structural self-organization of carbon nanotubes into vertically aligned networks of nanotube bundles

Bernard K. Wittmaack ^a, Abu Horaira Banna ^b, Alexey N. Volkov ^b, Leonid V. Zhigilei ^{a,*}

^a Department of Materials Science and Engineering, University of Virginia, 395 McCormick Road, Charlottesville, VA 22904-4745, USA

^b Department of Mechanical Engineering, University of Alabama, Hardaway Hall, 7th Avenue, Tuscaloosa, AL 35487, USA



ARTICLE INFO

Article history:

Received 26 August 2017

Received in revised form

19 December 2017

Accepted 20 December 2017

Available online 22 December 2017

ABSTRACT

An effective and flexible method for the generation of computational samples for mesoscopic modeling of anisotropic networks of carbon nanotube (CNT) bundles with various degrees of CNT alignment is developed and applied for investigation of structural self-organization of nanotubes into vertically aligned CNT forests and fibers. Structural characteristics of the computational samples, such as bundle size distribution, average and maximum bundle sizes, magnitude of the Herman orientation factor, average tilt of CNT segments with respect to the direction of alignment, and average tortuosity of the nanotubes, are calculated and related to parameters of the sample preparation procedure. Good agreement between the computer-generated and experimentally-grown network structures is demonstrated, and several examples of the applications of the mesoscopic modeling for investigation of mechanical and thermal transport properties of the CNT materials are provided. The high degree of control over the structure of computational samples, provided by the sample generation procedure, enables fine-tuning of the structural characteristics of *in silico* generated samples to match those to particular experimental materials, as well as an efficient exploration of the multidimensional space of structural parameters aimed at optimization of mechanical and transport properties and establishing structure – property relationships for this important class of network materials.

© 2017 Elsevier Ltd. All rights reserved.

1. Introduction

Carbon nanotube (CNT) materials possess an attractive combination of structural, mechanical, and transport properties, and continue to hold high promise for a broad range of practical applications [1,2]. Two types of CNT materials with pronounced directional anisotropy, vertically aligned carbon nanotube (VACNT) arrays and CNT fibers, are of particular interest for applications with stringent requirements for the mechanical strength, toughness, and thermal energy dissipation.

The VACNT arrays, also known as VACNT “forests,” [3–5] are typically composed of long (up to centimeters [5]) CNTs extending through the whole length of the arrays. These materials are usually produced by chemical vapor deposition (CVD) [6–13], where a hydrocarbon gas reacts with catalytic metallic nanoparticles and decomposes to provide carbon for continuous growth of CNTs. The mass density, types and diameters of constituent CNTs, nanotube

areal density, and the mesoscopic structure of VACNT arrays can be strongly affected by the CVD growth conditions [8–10], type, size, and dispersion of the catalyst nanoparticles [11], as well as the properties of the substrate [12,13]. The VACNT arrays have been shown to exhibit a unique combination of mechanical resilience (ability to support large reversible deformation and absorb mechanical energy) and high anisotropic thermal conductivity in the direction of CNT alignment [14], which makes them good candidates for applications requiring both heat management and mechanical energy dissipation.

Another type of anisotropic CNT materials deriving their properties from a high degree of structural anisotropy are CNT fibers [15–20], where nanotubes are spun together into ropes or yarns. In contrast to VACNT arrays, individual CNTs in the fibers do not extend throughout the length of the fibers, but are woven into continuous network structures exhibiting high degrees of nanotube alignment. The fibers are either directly fabricated through spinning from the synthesis reaction zone [21] or produced from pre-made CNTs by wet spinning combined with twisting and solution-based densification [19,22], mechanical stretching of random CNT

* Corresponding author.

E-mail address: lv2n@virginia.edu (L.V. Zhigilei).

networks [23,24], or other methods. With proper structural optimization, the CNT fibers have been shown to exhibit tensile strength as high as ~8.8 GPa [21], impressive strain hardening exceeding that of annealed low-carbon steel by more than a factor of three [23], and ultrahigh conductivity [19].

The mechanical and transport properties of both CNT forests and fibers are highly sensitive to the arrangement of individual CNTs into mesoscopic structural elements of the network materials, such as CNT bundles and branching structures, which produces materials characterized by different bundle size distribution, porosity, and the degree of nanotube entanglement. The structural characteristics of CNT networks are not uniquely defined by the length and flexural rigidity of CNTs and material density, but can be modulated by changing the parameters of the production process, mechanical and chemical post-processing, radiative treatment, etc. In the case of CNT fibers fabricated, e.g., by the direct spinning method, the degree of CNT alignment as well as the size and morphology of pores can be modulated in broad ranges by varying the so-called drawing ratio between the extraction rate of the fiber from a reactor and carrier gas velocity [25]. The empirical exploration of the broad space of structural parameters of anisotropic CNT network materials is challenging [8,26] and the structural optimization can be greatly assisted by computer modeling targeting the structure – properties relationships.

The complexity and inherently multiscale nature of the structural organization of the CNT network materials suggest that complete understanding of the connections between the structural parameters and the effective (macroscopic) properties of these materials can only be achieved through a combination of various computational techniques. In particular, the atomistic molecular dynamics (MD) technique [27] is well suited for simulation of the mechanical and thermal transport properties of individual nanotubes, e.g., [28–39], and small groups of CNTs, e.g., [24,40–43]. The information gained from the atomistic simulations can be used for parameterization of mesoscopic models that adopt simplified representations of nanotubes [44–47] and are capable of simulating the collective behavior and properties of large CNT ensembles, e.g., [45,47–50]. The results of the mesoscopic simulations can be, in turn, used for revealing general trends and formulating continuum-level constitutive relations that describe the macroscopic behavior and properties of the CNT network materials.

In the atomistic – mesoscopic – continuum chain of the multiscale computational treatment of CNT materials, the “weak member” is the mesoscopic modeling. While the atomistic and continuum models are well established and implemented in user-friendly computational software packages, the general framework of the mesoscopic computational treatment of nanotube materials is still being developed, validated, and redesigned. Several alternative approaches for mesoscopic modeling of CNT materials have been suggested in literature. One of the early models developed by Buehler [44] is based on the bead-and-spring model commonly used in simulations of polymers [51]. In this model, the van der Waals inter-tube interactions are represented through spherically symmetric pair-wise interactions between mesoscopic nodes arranged along the axes of nanotubes. Due to its simplicity and straightforward implementation, the bead-and-spring model has been adopted by several groups and used in a number of investigations of the structural and mechanical properties of CNT films [48,52–58] and VACNT arrays [59]. The model, however, suffers from large artificial barriers for relative displacements of neighboring CNTs introduced by the pair-wise interactions between the “beads” in the bead-and-spring model. As discussed in Refs. [45,47,49,60], the presence of these barriers prevents long-range rearrangements of CNTs into continuous networks of bundles and strongly affects the structure and mechanical behavior of

the CNT materials. More recently, a finite element model [61] describing van der Waals inter-tube interactions by linear elastic bar elements added at localized “contacts” has been proposed and applied for simulation of mechanical behavior of two-dimensional CNT forests. The description of CNT-CNT interaction by strong localized bonds that cannot be broken in the course of the forest “growth” or compressive deformation casts doubt on the ability of the model to provide an adequate description of the structural self-organization or mechanical properties of the CNT materials.

More advanced descriptions of non-bonding inter-tube interactions that do not result in the artificial corrugated inter-tube interactions have been developed and include a mesoscopic model [45,62,63] based on the distinct element method [64,65] and a model representing nanotubes as a sequence of cylindrical segments [46] interacting with each other through the tubular potential method [47]. The latter approach has been parametrized to provide a realistic description of nonlinear deformation, buckling [49,66] and mechanical energy dissipation in individual CNTs [67], as well as collective heat transfer in CNT materials [41,50,66,68]. This model is briefly described below, in section 2, and is used in the present paper for simulation of structural self-organization of CNTs into partially aligned networks of bundles in VACNT arrays and CNT fibers. A method for *in silico* preparation of structurally distinct VACNT arrays based on the variation of the initial inclination of nanotubes with respect to the direction of alignment and the annealing temperature is described in section 3. The results of the structural characterization of VACNT arrays of different density are presented and related to the sample preparation procedure in section 4. The effect of CNT length on the structure of VACNT arrays is considered in section 5. The method developed for generation of VACNT arrays is extended to CNT fibers in section 6. Several examples of the applications benefiting from the fine control over mesoscopic structure of VACNT samples enabled by the developed sample preparation method are provided in section 7, and the results are summarized in section 8.

2. Mesoscopic force field model for carbon nanotube materials

The mesoscopic force field model developed for realistic large-scale simulations of CNT materials is based on a coarse-grained representation of individual CNTs as chains of stretchable cylindrical segments [46]. The state of each segment is defined by positions, velocities, and internal temperatures of nodes joining the neighboring segments [46,47]. The dynamics of a system of interacting CNTs is described by solving the equations of motion of classical mechanics for the positions of all nodes [46], as well as the heat transfer equations for the internal thermal energy associated with the nodes [66,68]. The forces acting on the nodes are calculated based on a mesoscopic force field that accounts for stretching and bending deformation of individual CNTs as well as for the van der Waals interactions among the CNTs.

The potential energy defining the mesoscopic force field is expressed as $U = U_{str} + U_{bnd} + U_{T-T} + U_E$, where U_{str} and U_{bnd} correspond to the strain energies associated with stretching and bending of individual CNTs, U_{T-T} is the energy of non-bonded inter-tube interactions, and U_E is the energy of interaction between nanotubes and external bodies. The latter term is used in this work to represent the substrate in simulations of VACNT arrays described in sections 3–5, as well as the indenter and projectile in simulations of uniaxial compression and particle impact discussed in section 7. The harmonic parts of the stretching and bending potentials, U_{str} and U_{bnd} , are parametrized for single-walled CNTs in Ref. [46] based on the results of atomistic simulations performed with the reactive empirical bond-order (REBO) potential [69,70].

The descriptions of the transition to the anharmonic regime (nonlinear stress-strain dependence), axial buckling of CNTs under uniaxial compression, and fracture of CNTs under tension are included in U_{str} but do not play any significant role under conditions of the simulations discussed in this paper. The bending buckling is also accounted for in U_{bnd} and, in contrast to the axial buckling, is found to play an important role in stabilization of the continuous networks of CNT bundles [49].

The inter-tube interaction term U_{T-T} is calculated based on the tubular potential method [47] that provides a non-corrugated description of relative sliding of nanotubes and accurately reproduces the van der Waals interactions between CNT segments of arbitrary lengths and orientation. The tubular potential is parametrized based on an interatomic potential for nonbonded interactions between carbon atoms used in the adaptive intermolecular REBO (AIREBO) potential [71] and is found to reproduce the predictions of the atomistic representation of the inter-tube interactions with high accuracy at a small fraction of the computational cost [47]. The mesoscopic force field does not include a description of forces related to inter-tube friction, as these forces are too weak to prevent room-temperature rearrangements of defect-free CNTs [72,73]. In particular, the values of static friction forces measured for pairs of annealed nearly perfect CNTs are found to be independent of the overlap area [73] and are consistent with forces originating from the changes in the inter-tube interaction area. These forces are naturally accounted for in the mesoscopic model.

The mesoscopic simulations of thermal transport properties of CNT materials are enabled by the descriptions of inter-tube thermal conductance [50], intrinsic conductivity of CNTs [68], and thermal resistance of buckling kinks [66]. The dissipation of mechanical energy of longitudinal and bending oscillations, *i.e.*, the energy transfer from low-frequency mechanical oscillations to high-frequency atomic vibrations that are not explicitly represented in the mesoscopic model, is accounted for in the model through a novel “internal heat bath” approach that couples the dynamic degrees of freedom of the mesoscopic model with internal energy of the corresponding nanotube segments [67]. The internal heat bath approach ensures a correct heat capacity of CNT materials in mesoscopic simulations and plays an important role in simulations of dynamic phenomena, such as the material response to impact loading or localized energy deposition. The model is implemented in a parallel computer code designed for large-scale simulations of CNT samples with dimensions of up to several micrometers.

The initial applications of the mesoscopic model have demonstrated the ability of the model to reproduce the self-organization of CNTs into continuous networks of bundles [47,49,60] with structural characteristics similar to the ones observed experimentally, revealed the critical role the bending buckling of CNTs plays in stabilization of the network structures [49], and provided important insights into the structural dependence of the thermal transport properties of the CNT network materials [50,60,66,68]. The methods developed in this paper for generation of realistic structures of VACNT arrays and CNT fibers will enable extension of the range of applications of the mesoscopic model to include investigation of structure – properties relationships in this important class of CNT materials.

3. Making VACNT forests *in silico*

A series of computational VACNT samples composed of single-walled carbon nanotubes (SWCNTs) and featuring distinct structural characteristics are generated and equilibrated using the mesoscopic force field model described in section 2. In order to produce realistic *in silico* SWCNT forests, the CNT diameter and

nanotube areal density (*i.e.*, the number of nanotubes grown on a unit area of the substrate) are selected to match those characteristic of experimentally grown VACNT arrays. The ranges of the CNT diameters and areal densities reported in literature for SWCNT forests grown by CVD are illustrated by several representative examples [74–78] in Fig. 1. Due to the narrow distribution of CNT diameters typically found in SWCNT forests [75–79], a constant diameter of 1.357 nm, characteristic of (10,10) CNTs [47], is selected for all nanotubes in the computational samples.

The CNT areal density of experimental samples illustrated in Fig. 1 exhibits a large, more than three orders of magnitude, variability. The areal density is an important parameter as it directly affects the structural characteristics of the network of bundles generated during the growth of a CNT forest. The balance between the inter-tube interaction energy and bending energy of CNTs, which defines the propensity of nanotubes to join the bundles or form interconnects between the bundles, is to a big extent controlled by the areal density of CNTs. To investigate the effect of the areal density on the structural characteristics of the CNT forests, the computational samples are generated in this work for two values of the areal density. Three samples, designated as FA, FB, and FC in Fig. 1, have an areal density of $6.09 \times 10^{11} \text{ cm}^{-2}$, and one denser sample, FD, has a five times higher areal density of $3.05 \times 10^{12} \text{ cm}^{-2}$.

Another important consideration is the choice of the length of CNTs. If the nanotubes are too short, then the degree of CNT-CNT interactions and connectivity of CNT networks is limited by the relatively large energy penalty associated with bending the nanotubes needed to form bundles. Computational treatment of very long nanotubes, however, is costly, as the number of dynamic units (nodes) for which the equations of motion are solved in mesoscopic simulations is proportional to the CNT length. The length of the nanotubes in the experimentally grown VACNT forests illustrated in Fig. 1 range from several micrometers to hundreds of micrometers, but the microstructural characteristics are already well-defined at the micrometer scale. Therefore, in order to cost-effectively reproduce the microstructure observed in experiments, the length of CNTs is chosen to be 2 μm in the computational VACNT samples considered in this section. The dependence of the structural characteristics of VACNT forests on the CNT length is discussed and illustrated by simulations performed for shorter, 200

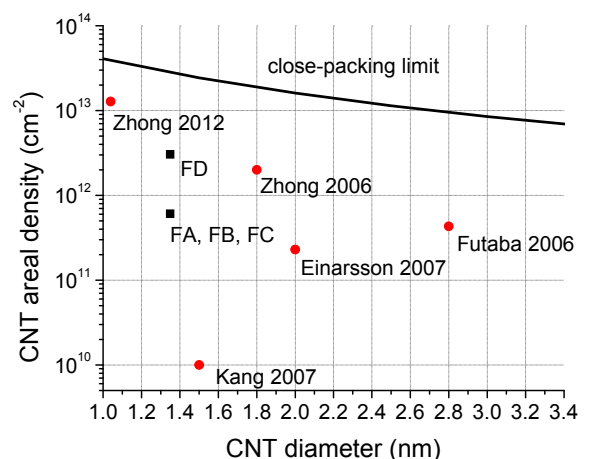


Fig. 1. Chart showing the areal densities and CNT diameters of five representative SWCNT forests grown by CVD (marked as Zhong 2012 [78], Kang 2007 [76], Zhong 2006 [74], Einarsson 2007 [77], and Futaba 2006 [75]) along with the four SWCNT forests generated *in silico* in this work (marked as FA, FB, FC, and FD). (A colour version of this figure can be viewed online.)

and 600 nm, forests in section 5.

Once the initial parameters are selected, there are two ways to proceed for making a realistic forest microstructure. Either the forest can be “grown” by lengthening the nanotubes over the course of a simulation [61] or the fully sized nanotubes can be made to self-organize [80]. We chose the latter option because it is more straightforward, and has already been proven to be effective in generation of CNT films, or “buckypaper,” with random orientation of nanotubes within the planes of the films [47–49].

As the first step of the sample generation, perfectly straight nanotubes are randomly placed on a substrate at a certain inclination with respect to the substrate surface normal (the choice of the inclination angle is discussed below). The positions of CNT segments (two nodes) adjacent to the substrate are fixed, so that these segments stay at their initial inclination during the self-organization of nanotubes into a network of bundles. In the course of the generation of the initial forest, a new CNT is only added to the sample if the minimum gap between the surfaces of the new and any of the CNTs already present in the sample is larger than the equilibrium distance of 3.14 Å [47]. If the new CNT is too close to an existing CNT, the nanotube is not added and another random location for the next CNT is selected. This acceptance-and-rejection process of the random generation of new nanotubes continues until a desired material density ρ is reached.

The random placement of the nanotubes on the substrate is done within a rectangular area of pre-defined dimensions. For all computational samples but sample FD, periodic boundary conditions are applied in the lateral directions, parallel to the surface of the substrate. These boundary conditions make it possible to represent VACNT forests extending much further than the actual lateral dimensions of the computational system. The choice of the lateral dimensions of the computational system is defined by the condition that the sample is sufficiently wide to ensure that any nanotube would not span more than half of the computational domain at any time during the simulation. This condition is more stringent than the requirement of the absence of CNT self-interactions and is imposed in this work to ensure that the structural characteristics of the generated samples are not affected by the periodic boundary conditions. Due to the difference in the maximum initial inclination of the nanotubes with respect to the substrate normal (see below), different lateral dimensions are chosen for samples FA, FB, FD ($0.64 \mu\text{m} \times 0.64 \mu\text{m}$), and sample FC ($12.82 \mu\text{m} \times 1.82 \mu\text{m}$). The parameters of the VACNT samples generated with 2-μm-long (10,10) CNTs are summarized in Table 1.

In our first attempt to generate CNT forests, all nanotubes are initially oriented perpendicular to the substrate, and the process of self-organization of CNTs into a network of bundles is induced by bringing the system to a high temperature, maintaining the temperature for 1 ns using the Berendsen thermostat algorithm [82], and then relaxing the sample at 300 K. A large fraction of the nanotubes (~55%), however, is found to remain isolated from any of the neighboring CNTs in samples with density of 0.02 g/cm^3 , even when the thermal annealing is performed at a temperature as high

as 10,000 K (the model does not include the possibility of thermal decomposition of CNTs, and the temperature is defined based on the average kinetic energy of mesoscopic dynamic units of the model). The relatively high bending energy associated with bringing the vertically-oriented nanotubes into bundles is preventing the formation of continuous networks of bundles, commonly observed in experiments [3–14,74–79,83,84], through the high temperature annealing alone.

In order to facilitate the formation of interconnected network of bundles, the algorithm used for the generation of VACNT arrays is modified by introducing a random inclination of the straight nanotubes relative to the substrate normal. This way, the nanotubes can more easily interact with each other during the high temperature stage of the sample preparation and join different bundles along the height of the forest. Moreover, we found that the maximum inclination of the CNTs can serve as a parameter that effectively controls the microstructure of the VACNT arrays. Thus, the three-step process developed for the generation of VACNT samples with tunable structural characteristics can be described as follows. First, a sample composed of straight nanotubes with initial inclinations with respect to the substrate normal chosen randomly in a range from 0° to a maximum angle Θ_{max} is generated. Then, the initial sample undergoes thermal annealing in a mesoscopic dynamic simulation performed at a temperature of 5000 K for 1 ns. During this high temperature stage, the initially straight and isolated nanotubes self-organize into a continuous network of bundles, as schematically shown in Fig. 2, where the shape of a representative nanotube before and after annealing is highlighted. Finally, the VACNT forest is quenched to 300 K and allowed to relax until a metastable configuration, defined as a state where the rate of change in the inter-tube interaction energy slows down to a level below 0.05% per ns, is reached. Note that the computational procedure described above cannot be directly mapped to laboratory conditions, where a variety of growth and post-processing procedures have been developed to control the degree of nanotube alignment in VACNT forests, e.g., Refs. [4,8,85,86]. Nevertheless, as demonstrated below, in sections 4–6, the choice of Θ_{max} can be used as an effective way to tune the structural characteristics of the computational samples and to reproduce the structure of experimental samples in the mesoscopic simulations.

The procedure described above is applied in this work for generation of three VACNT forests with density of 0.02 g/cm^3 and one forest with a higher density of 0.1 g/cm^3 . The parameters of the four samples are provided in Table 1. The structure of the low-density forests is controlled by the maximum initial inclination of the nanotubes, Θ_{max} , chosen to be 0.6° , 12° , and 27° in the three forests denoted as FA, FB, and FC, respectively. The VACNT forest with a density of 0.1 g/cm^3 , five times greater than that of the other three forests, is prepared using the same method and the maximum inclination of 0.6° , i.e., the same as in the sample FA. This higher-density sample is denoted as FD in Table 1 and further discussion. The results of the structural characterization of the four VACNT forests are presented in the next section.

Table 1
Parameters of CNT forests generated in the mesoscopic simulations. The CNT spacing is defined as center-to-center distance assuming hexagonal packing of the nanotubes. Data files defining the structures of computational samples listed in this table are accessible from Ref. [81].

Forest	Density (g/cm^3)	Areal density (cm^{-2})	Volume occupancy	CNT spacing (nm)	CNT length (μm)	Lateral size ($\mu\text{m} \times \mu\text{m}$)	Number of CNTs	Max. initial inclination Θ_{max} (deg.)
FA						0.64×0.64	2498	0.6°
FB	0.02	6.09×10^{11}	0.9%	13.77	2	0.64×0.64	2498	12°
FC						1.82×1.82	20,438	27°
FD	0.1	3.05×10^{12}	4.52%	6.16	2	0.64×0.64	12,676	0.6°

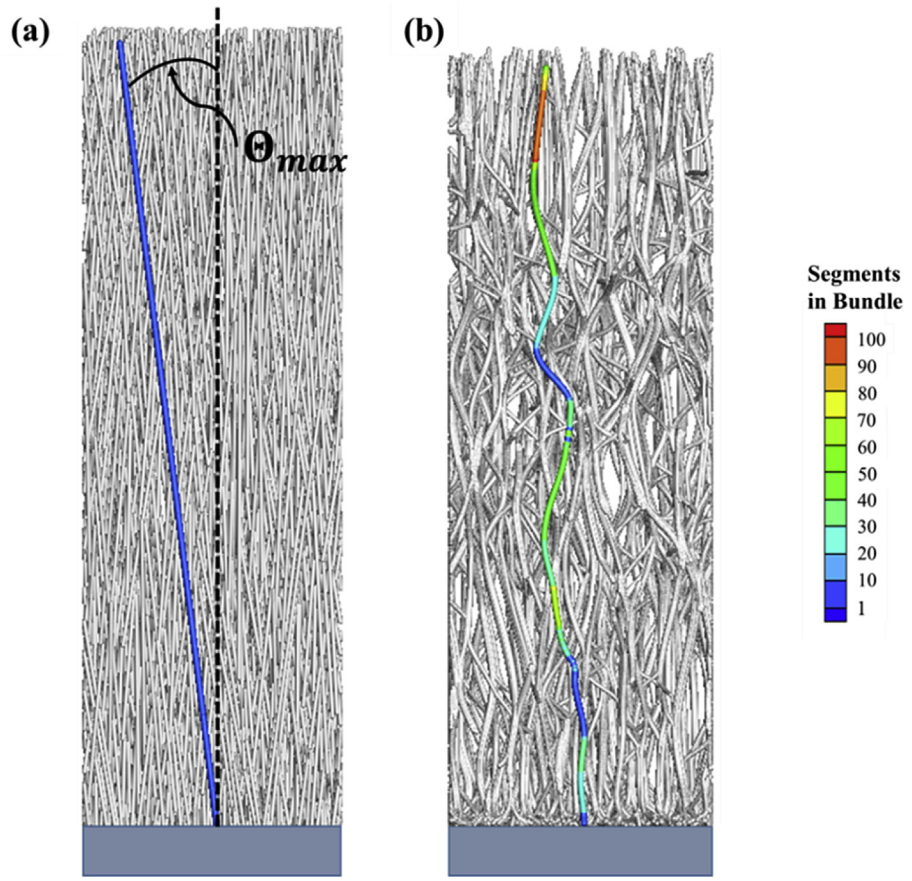


Fig. 2. Schematic representation of the procedure used for the generation of VACNT samples. Straight CNTs are first randomly placed on a substrate with a random inclination with respect to the substrate normal Θ , ranging uniformly from zero to a maximum angle Θ_{max} (a). The high temperature annealing followed by a relaxation at 300 K is used to induce self-organization of CNTs into a continuous metastable network of interconnected bundles (b). A single representative nanotube is highlighted, colored by its local bundle thickness, and shown in front of the other nanotubes. All other nanotubes are colored gray. (A colour version of this figure can be viewed online.)

4. Structural characteristics of VACNT forests

The visual views of three lower-density VACNT forests generated *in silico* as described above are provided in Fig. 3, where the

CNT segments are colored by local thickness of bundles they belong to. The bundle thickness is defined as the number of CNTs in a bundle cross section. Therefore, an isolated CNT segment has a bundle thickness of one and is colored blue in Fig. 3. Despite having

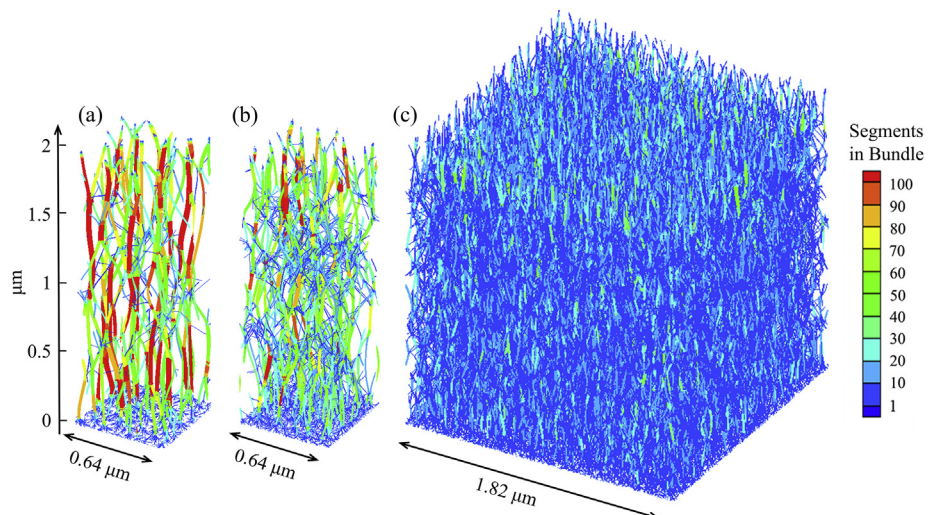


Fig. 3. Side views of computational samples of forests FA (a), FB (b), and FC (c) generated in mesoscopic simulations. The CNT segments are colored by the local bundle thickness (number of segments in a bundle cross section). Data files defining the structures of the computational samples shown in this figure are accessible from Ref. [81]. (A colour version of this figure can be viewed online.)

the same average density and being composed of CNTs of the same length and type, the three VACNT forests have distinct structures characterized by different thicknesses of nanotube bundles and densities of interconnects between the bundles. The nanotubes are assembled into fewer number of thicker bundles in sample FA, the bundles are the thinnest and most numerous in forest FC, while forest FB is intermediate between these two extremes.

The degree of interconnection between the bundles in the network structures of VACNT forests can be characterized by the extent to which individual nanotubes are parts of multiple bundles. Visually, the difference between the forests' morphologies can be seen from Fig. 4, where enlarged views of the network structures are shown for each of the three forests. It is apparent from Fig. 4 that, on average, CNTs in sample FC tend to be parts of larger number of bundles as compared to samples FB or FA. This observation is not surprising given the initial inclinations of the nanotubes in each sample, but has important implications for mechanical and thermal properties of the forests.

The structural differences between computational samples generated with different initial maximum inclinations of CNTs can be quantified by considering bundle thickness distributions shown for the three samples in Fig. 5a–c. The bundle thickness distributions calculated for samples FA and FB are qualitatively similar, although the distribution is narrower and shifted to smaller bundle sizes in sample FB. In sample FC, a big fraction of the nanotube segments (~16%) are not in contact with other segments. However, as can be seen from Fig. 4, this is the result of nanotubes spanning across the sample and participating in multiple bundles connected by isolated portions of CNTs, rather than entire CNTs remaining isolated from the neighboring CNTs. The maximum thickness of bundles found in the simulated network structures FA, FB, FC is equal to 230, 162, and 70 nanotube segments, respectively.

The structures of the computational samples can be related to the results of experimental analysis of the bundle thickness distribution in a VACNT forest of comparable density (0.035–0.05 g/cm³), reported in Ref. [77] and reproduced in Fig. 5d. Experimentally, the bundle thickness distributions were determined through inspection of transmission electron microscope (TEM) images of VACNT forests composed of 2-μm-long SWCNTs. The filled bars in Fig. 5d correspond to the bundles where the number of CNTs can be reliably counted based on the TEM images and the unfilled bars are the estimates based on the bundles where the number of CNTs was not clear from the images.

The fraction of individual (isolated) CNTs in the computational sample FC (Fig. 5c) is close to that in the experimental VACNT forest, ~15%, while the width of the distribution is almost twice wider in the computational sample than in the experimental one. Although the agreement between the experimental and computational

bundle size distributions in Fig. 5c and d are only semi-quantitative, we note that the thickness of the CNT bundles and other structural characteristics can be effectively controlled by the CNT synthesis parameters in experiments [4,8,85,86] and by the choice of the initial maximum inclination angle Θ_{max} in the computational procedure. Two laboratory-grown SWCNT forests are shown in Fig. 6. The sample shown in Fig. 6a [77] is the one used in the analysis of the bundle size distribution illustrated by Fig. 5d. As discussed above, bundle size distribution and overall structure of this forest are similar to those of the computer-generated sample FC. Another CVD grown forest of similar density (0.03 g/cm³), shown in Fig. 6b [75], exhibits thicker bundles and a remarkable visual similarity to the computational sample FA. Both the *in silico* and laboratory-grown forests in Fig. 4a and Fig. 6b are characterized by similarly sized and oriented bundles. Interestingly, since the three computational samples, FA, FB, and FC, have the same basic parameters (material density, length and type of the CNTs), the results of the simulations suggest that the forest morphology is not uniquely dictated by the nominal parameters of the CNT network material, but can be altered to a large degree by the sample preparation method.

The ability to accurately control the microstructure of computer-generated VACNT forests can be further evaluated by performing statistical analysis of the connection between the initial maximum CNT inclination angle Θ_{max} and the resulting structural characteristics of the anisotropic networks. The structural characteristics of the computational samples FA, FB, and FC are summarized in Table 2 and include the average tilt of CNT segments with respect to the direction of VACNT alignment $\langle \theta \rangle$, average bundle size $\langle N_B \rangle$, maximum bundle size N_B^{max} , standard deviation (SD) of the bundle size, and magnitude of the Herman orientation factor (HOF) defined as $S = \frac{1}{2} [3\langle \cos^2 \theta \rangle - 1]$, where θ is the local angle between a nanotube and the vertical axis, and the angle brackets $\langle \rangle$ denote averaging over all CNT segments in a sample. The HOF quantifies the extent of the orientation of nanotubes with respect to an axis of interest, and ranges from −0.5 to 1, where values of −0.5, 0, and 1 correspond to perpendicular alignment, isotropic orientation, and parallel alignment with respect to the axis, respectively.

Remarkably, all of the structural parameters of the three samples listed in Table 2 exhibit nearly linear dependences on the maximum inclination angle Θ_{max} , as shown by the nearly perfect values of the corresponding coefficients of determination (R^2). The clear statistical link between the structural material parameters and Θ_{max} suggests that the sample preparation procedure described in section 3 can be used to precisely engineer the microstructure of a VACNT forest to match that of an experimental material of interest.

Finally, the effect of material density on the structural

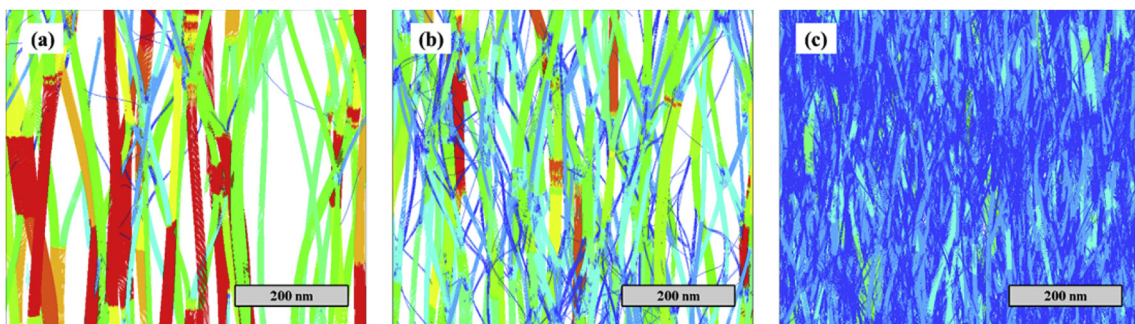


Fig. 4. Enlarged views of computational VACNT forests FA (a), FB (b), and FC (c) illustrating the degree of interconnection among the bundles. The coloring scheme is the same as in Fig. 3. (A colour version of this figure can be viewed online.)

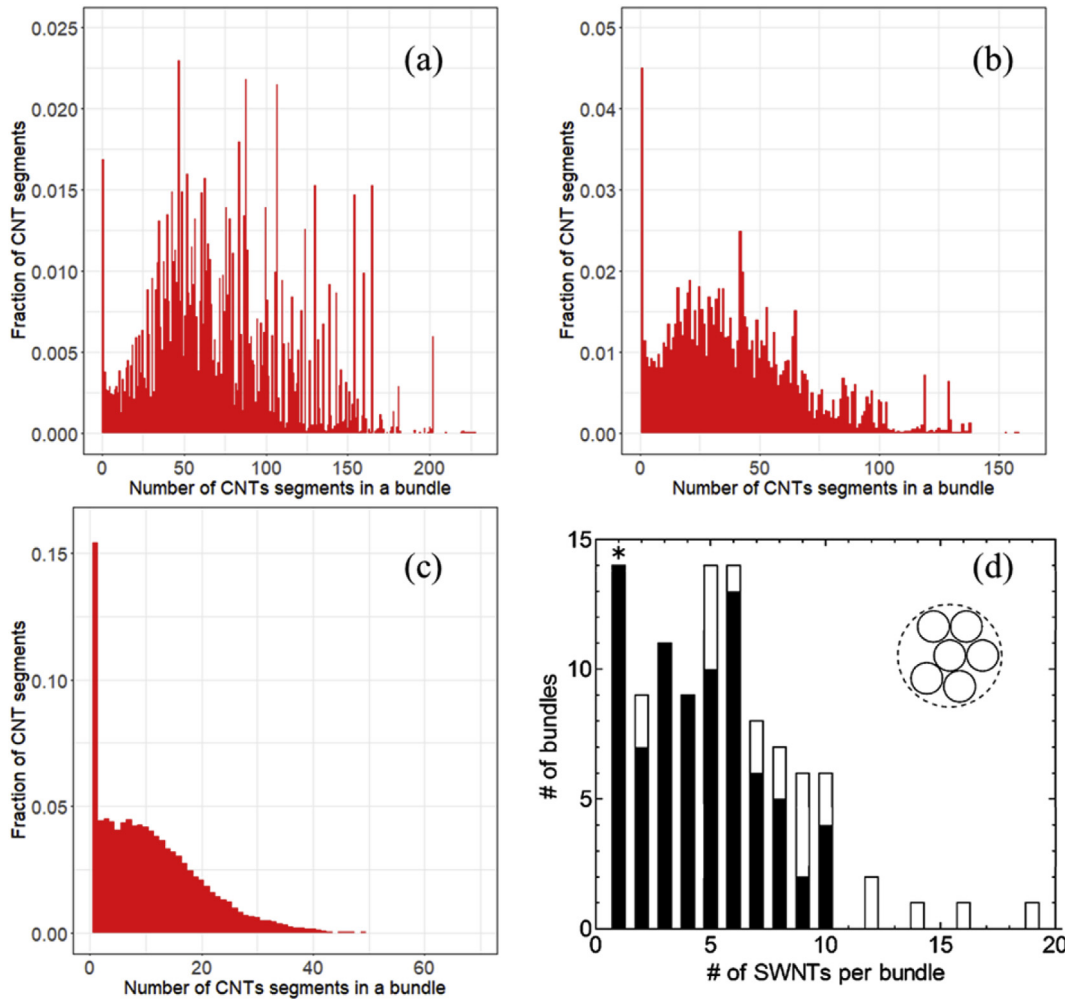


Fig. 5. The bundle thickness distributions calculated for computational samples FA (a), FB (b), and FC (c), as well as for a laboratory-grown forest analyzed in Ref. [77] (d). In the computational and experimental CNT forests, the bundle thickness is expressed in the number of nanotubes present in bundle cross sections, and each bin covers a thickness increment by 1 CNT segment. In (d), the filled bars are for SWCNT bundles where the number of nanotubes can be reliably counted in TEM images, while the unfilled bars are estimates based on the visual thickness of the bundle. The star marks the number of isolated SWCNTs, and could be higher than the estimate shown in the figure. (A colour version of this figure can be viewed online.)

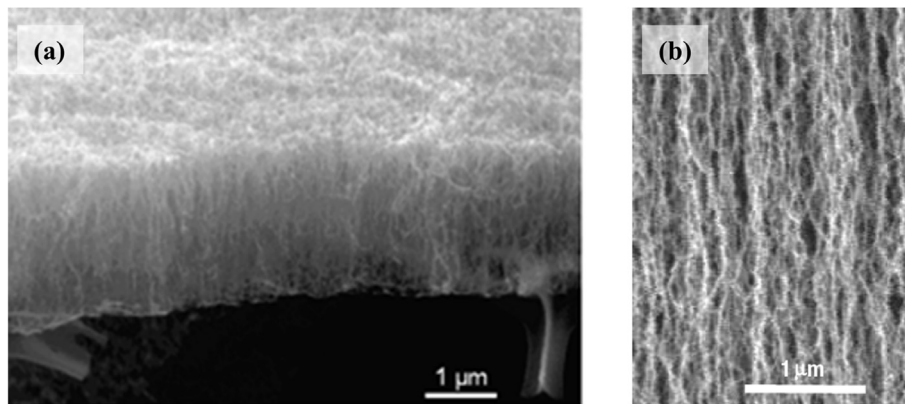


Fig. 6. Scanning Electron Microscopy (SEM) images of CVD grown SWCNT forests with smaller [77] (a) and larger [75] (b) nanotube bundles.

characteristics of computer-generated VACNT structures can be evaluated by considering the higher density sample FD. Although the density of this sample (0.1 g/cm^3 or $3.05 \times 10^{12} \text{ cm}^{-2}$) is about an order of magnitude below the close-packing limit and does not

quite compare with the densest laboratory-grown forests produced by advanced growth techniques [78,83,84] or post processing methods [75], it nonetheless is higher than density of majority of VACNT forests reported in literature, e.g., Fig. 1. The visual

Table 2

Statistical information on the structural parameters of three computational forests of the same density of 0.02 g/cm^3 . The average tilt of CNT segments ($\langle \theta \rangle$), average bundle size ($\langle N_B \rangle$), maximum bundle size N_B^{max} , standard deviation (SD) of the bundle size, and magnitude of the Herman orientation factor (HOF) are listed for computational samples FA, FB, and FC. The coefficients of determination R^2 are listed for linear dependencies of the structural parameters on Θ_{max} .

Sample [Θ_{max}]	$\langle \theta \rangle$	$\langle N_B \rangle$	N_B^{max}	SD	HOF
FA [0.6°]	13.7°	77	230	43	0.88
FB [12°]	17.6°	42	163	28	0.82
FC [27°]	19.4°	12	70	9	0.79
R^2	0.92	0.98	1.00	1.00	0.93

inspection of the microstructure of sample FD shown in Fig. 7a and b suggests that the size of bundles is comparable to that of sample FA, Fig. 3a and Fig. 4a. Indeed, despite the five times higher density of sample FD, the bundle size distribution shown in Fig. 7c is similar to the distribution shown for sample FA in Fig. 5a. The forest FD has an average bundle thickness of 71, very close to that of 77 calculated for FA, although the maximum number of segments in a bundle for FD is 301 compared to 230 for FA. The more densely packed structure of sample FD, however, is characterized by higher degree of vertical alignment, with the average angle between the CNT segments and the vertical axis, $\langle \theta \rangle$, equal to 8.4° , and the magnitude of HOF equal to 0.95. The results of the structural characterization of sample FD agree well with the correlation between density and the degree of CNT alignment observed in laboratory-grown forests [4], and imply that at high densities, the variation of microstructure exhibited by CNT forests is more constrained by crowding of the nanotubes.

5. The effect of CNT length in short VACNT forests

All the results discussed above are for VACNT forests composed of 2-μm-long CNTs, where the effects of the substrate and free surfaces of the VACNT arrays on the structural organization of the networks of bundles is limited to relatively shallow bottom and top layers of the samples (Fig. 3), while the internal structure can be assumed to be largely unaffected by the finite length of the CNTs. The length effect, however, can be expected to be more significant for shorter VACNT arrays, warranting an investigation of the length dependence of the VACNT structures presented in this section.

To reveal the length dependence of the structural parameters of

the VACNT forests, two additional sets of VACNT forests composed of nanotubes with lengths of 200 nm and 600 nm are prepared using the method described in section 3. The initial VACNT samples are cubic, i.e., have dimensions of $200 \times 200 \times 200 \text{ nm}^3$ and $600 \times 600 \times 600 \text{ nm}^3$. In each set, three samples of the same areal density of $6.09 \times 10^{11} \text{ cm}^{-2}$ are prepared with initial maximum CNT inclinations of 0.6, 12, and 27° . Except for the CNT length, all other parameters of the sample preparation procedure are identical to the ones used in the generation of samples FA, FB, and FC discussed in the previous section.

The relaxed structures of the samples generated with 200- and 600-nm-long nanotubes are shown in Fig. 8. Here we notice that, regardless of the initial inclination, the shortest (200 nm) forests do not display the complex morphology of the 2-μm-long samples (Fig. 3), but rather form smaller and largely isolated bundles even when the initial maximum inclination of CNTs is 27° . The limited connectivity between the bundles in this case cannot be enhanced by further increase of the maximum inclination angle, as the lateral divergence from the point of origin on the substrate that corresponds to $\Theta = 27^\circ$ is about 91 nm for a 200-nm-long straight CNT, which is more than 6 times larger than the characteristic distance between the CNTs on the substrate (see Table 1). Thus, the virtual absence of participation of CNTs in multiple bundles is not related in this case to the lack of initial interactions, but is defined by the high bending energy penalty associated with the formation of interconnects between the bundles at such a short length-scale. Indeed, the characteristic length of branching of CNT bundles in Figs. 3 and 4, and well as the typical length of nanotube segments participating in different bundles that can be seen for the nanotube highlighted in Fig. 2, are both exceeding 200 nm.

When the height of the forest is increased to 600 nm, the degree of interconnection between the CNT bundles increases (Fig. 8d–f), and the structures become more similar to those observed for 2-μm-long forests (Fig. 3). The sample with the smallest maximum inclination angle of $\Theta_{max} = 0.6^\circ$ still exhibits mostly straight bundles with a rather limited degree of interconnection between the bundles (Fig. 8d). This observation can be explained by the limited initial interaction between the inclined nanotubes, as the maximum lateral divergence from the point of origin on the substrate that corresponds to $\Theta = 0.6^\circ$ is only 6.2 nm for a 600-nm-long straight CNT, which is more than twice smaller than the spacing between the CNTs on the substrate (see Table 1). As a result, the nanotubes are mostly forming bundles with their nearest neighbors and are unlikely to participate in multiple bundles, thus

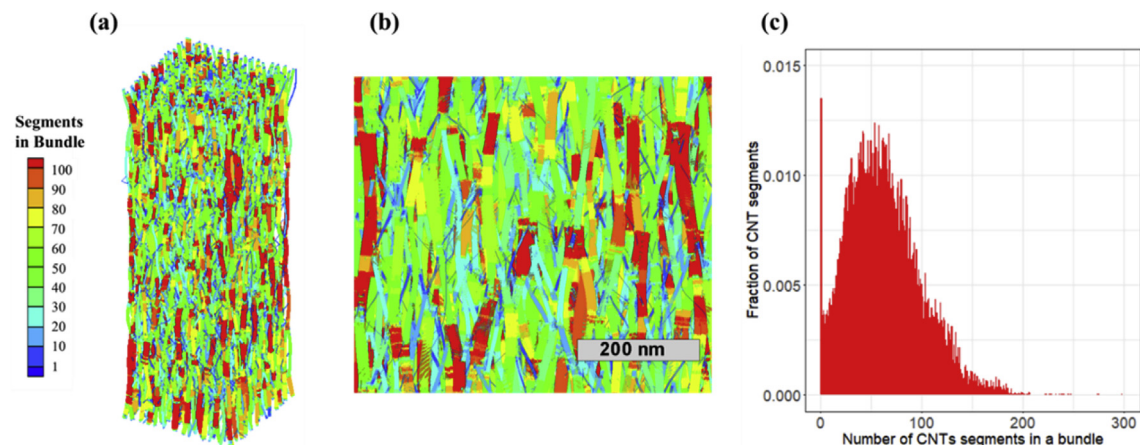


Fig. 7. The overall view (a), an enlarged fragment (b), and the bundle thickness distribution (c) of the computational sample FD. In (a) and (b), the CNT segments are colored by the local bundle thickness (number of segments in a bundle cross section), and in (c) each bin covers a thickness increment by 1 CNT segment. Data file defining the structure of the computational sample shown in this figure is accessible from Ref. [81]. (A colour version of this figure can be viewed online.)

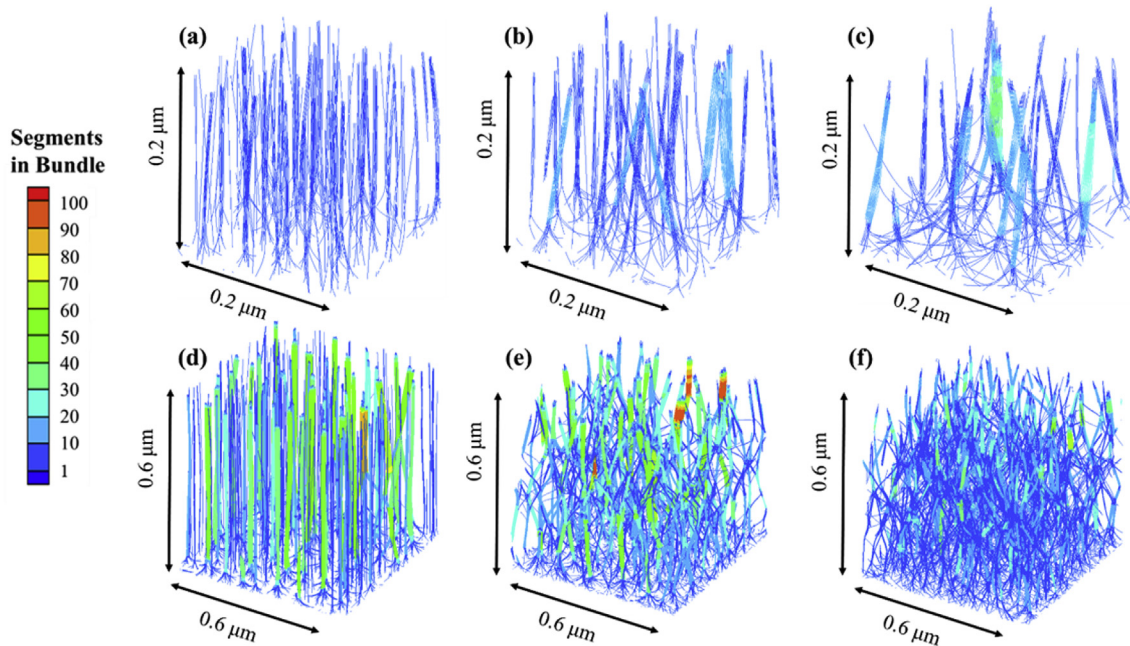


Fig. 8. Side views of computational VACNT samples composed of nanotubes with lengths of 200 nm (a–c) and 600 nm (d–f) generated in mesoscopic simulations according to the procedure described in section 3. The CNT segments are colored by the local bundle thickness (number of segments in a bundle cross section). (A colour version of this figure can be viewed online.)

limiting the degree of inter-bundle connectivity in the VACNT array shown in Fig. 8d. In samples generated with larger maximum inclination angles, Fig. 8e and f, the nanotubes do participate in multiple bundles and self-organize into interconnected networks of bundles similar to those obtained for longer forests and discussed in section 4.

The discussion based on the visual analysis of the computer-generated samples can be supported by quantitative analysis of the structural characteristics provided in Table 3 for the 200 and 600 nm VACNT forests. Both the average and maximum bundle sizes, $\langle N_B \rangle$ and N_B^{max} , are smaller in the samples generated with 200- and 600-nm-long CNTs, as compared to the 2-μm-long VACNT samples discussed in section 4 and listed in Table 2. The gap in the bundle sizes is particularly large for the shorter 200 nm VACNT forests, but decreases with increasing Θ_{max} for both sets of samples. The structural parameters listed in Tables 2 and 3 become similar in all three sets of the samples generated at the largest maximum inclination angle of 27°, although the structure of the shortest VACNT array is still visually distinct, as apparent from comparison of snapshots shown in Fig. 3c, Fig. 4c and Fig. 8c and 8f. Interestingly, the similar bundle sizes at the largest Θ_{max} are approached through different trends observed for the 200-nm-long forests,

where $\langle N_B \rangle$ and N_B^{max} increase with increasing Θ_{max} , and the 600-nm-long forests, where the bundle sizes decrease with increasing Θ_{max} (the non-monotonous dependence of N_B^{max} on Θ_{max} for 600 nm VACNT array can be attributed to the high susceptibility of N_B^{max} to statistical fluctuations). The latter trend is similar to the one observed for the 2-μm-long forests (see Table 2), suggesting that the factors controlling the structural parameters of the 600-nm-long and 2-μm-long forests are similar.

Overall, we can conclude that while it is possible to produce short VACNT arrays with the average structural parameters similar to those of longer VACNT forests, the network structures characterized by interconnected bundles and typically observed in experiments [3–14,74–79,83,84] can only be built of CNTs that are ~300–500 nm or longer. The distinct structure of the short VACNT arrays observed in the simulations is not a result of the limitations of the computational sample preparation procedure, but a reflection of the natural energy minimization in forests consisting of short nanotubes.

6. Generation of CNT fibers

The computational methodology developed in section 3 for generation of VACNT forests is extended here to the preparation of CNT fibers composed of nanotubes that have preferential orientation along a selected direction. Similarly to the computational samples of “buckypaper” investigated in a number of earlier studies, e.g., Refs. [44,45,47–50,52–58], the length of individual nanotubes in the CNT fibers is assumed to be smaller than the size of the computational system, and the nanotubes are arranged into a continuous network of bundles. In contrast to the VACNT arrays where one end of each nanotube is fixed at the substrate, in the CNT fibers both ends of the CNTs are free to move during the self-organization into the network structure. The absence of fixed CNT ends in the CNT fibers increases mobility of individual nanotubes and sets a lower limit on the range of the material density where stable continuous networks can be obtained. The minimum density that ensures formation of a stable network structure depends on the

Table 3

Statistical information on structural parameters of six computational forests of the same density of 0.02 g/cm³ composed of CNTs with lengths L_{CNT} of 200 nm and 600 nm. The average tilt of CNT segments (θ), average bundle size $\langle N_B \rangle$, maximum bundle size N_B^{max} , standard deviation (SD) of the bundle size, and magnitude of the Herman orientation factor (HOF) are listed for computational samples generated at maximum inclination angles Θ_{max} of 0.6°, 12°, and 27°.

Sample: L_{CNT} , Θ_{max}	$\langle \theta \rangle$	$\langle N_B \rangle$	N_B^{max}	SD	HOF
200 nm, 0.6°	5.6°	4	10	3	0.96
200 nm, 12°	11.5°	7	24	5	0.89
200 nm, 27°	20.5°	10	36	9	0.73
600 nm, 0.6°	5.7°	28	82	19	0.95
600 nm, 12°	17.2°	22	98	18	0.82
600 nm, 27°	22.9°	10	65	9	0.72

CNT length, i.e., the longer are the nanotubes, the lower is the density limit for the generation of stable network structures. In particular, the results of our mesoscopic simulations performed for three-dimensional isotropic CNT networks composed of 400-nm-long CNTs reveal that, in the absence of CNT defects and inter-tube cross-links, the networks are unstable for densities smaller than $\sim 0.0025 \text{ g/cm}^3$. In the discussion below, the procedure of generation of computational samples is illustrated for fibers composed of 400-nm-long (10,10) CNTs and having a material density of 0.01 g/cm^3 . Although the increasing degree of alignment of CNTs along the fiber axis reduces stability of network structures at a given material density, we found that CNTs form metastable networks in all of the fiber samples considered in this work. This ability of CNTs to form low-density continuous metastable networks is in agreement with experimental studies, where, according to review [20], stable CNT fibers are reported for a density range from 5.5×10^{-4} to 2.16 g/cm^3 . The results of the structural characterization of CNT fibers generated *in silico* are related to experimental data reported for low-density CNT fibers produced, e.g., by the direct spinning method [25]. Since the detailed results of experimental characterization of low-density CNT fibers are scarce, we also make connections between structural properties of our computational samples and experimental data reported for CNT fibers of medium density, e.g., [16].

The initial samples of CNT fibers composed of straight and dispersed CNTs are prepared by the acceptance-and-rejection method described in section 3. In contrast to the generation of VACNT arrays, where the CNTs were attached to the substrate on one end and formed a free surface on another end of the sample, the periodic boundary conditions are applied in all three directions for the generation of continuous (infinitely-long) CNT fibers. The positions of centers of CNTs, which are sequentially added to the system, are chosen at random within the simulation box, and the directions of CNT axes are randomly picked from a uniform distribution within a cone with the apex angle Θ_{max} with respect to the predefined axis of the fiber. A new CNT is added to the sample only if the minimum gap between the surfaces of the new and any of the CNTs already present in the sample is larger than a predefined minimum distance. In contrast to the procedure used for the generation of VACNT arrays, where the minimum distance was selected to be equal to the equilibrium distance between nanotubes, i.e., 3.14 \AA for (10,10) CNTs (see section 3), the minimum distance in the generation of CNT fibers was set to be equal to 3 \AA . As a result, the initial samples contain a certain fraction of pairs of CNTs experiencing inter-tube repulsive force. This initial repulsive interaction is sufficient for triggering self-assembly of CNTs into a network even in a constant-volume and constant-energy simulation, without the temperature control through a computational thermostat.

The approach to the generation of the computational samples developed in the present work is characterized by an inherent limit on the maximum density of the CNT networks. The large excluded volume of high-aspect ratio nanotubes makes it impossible to produce materials above a certain density based on the initial distribution of straight non-aligned nanotubes. In particular, we found that it is not possible to generate cubic samples of $1 \mu\text{m}^3$ in volume composed of 400-nm-long CNTs with material densities higher than 0.1 g/cm^3 . The larger material densities, however, can be achieved through gradual densification (reduction of all or some of the dimensions of the computational cell) in the course of the initial self-organization of CNTs into a network or a subsequent thermal annealing of low-density network structures. Using this approach, we were able to obtain relaxed samples of CNT fibers with densities up to 0.6 g/cm^3 . Such super-aligned fiber structures will be discussed in detail elsewhere.

Several representative configurations of the CNT fibers generated with an approach described above for material density of

0.01 g/cm^3 and different maximum angles of initial inclination, Θ_{max} , varying from 3° to 45° , are shown in Fig. 9. The *in silico* sample preparation procedure consists of a 3-ns-long high-temperature stage, when the “mesoscopic” temperature of the system (see comment on the temperature of the mesoscopic system in section 3) is kept at a level of 10,000 K, followed by a relaxation stage at a temperature of 300 K, both performed using the Berendsen thermostat algorithm [82]. The high-temperature stage leads to the fast formation of a continuous network structure, while the relaxation stage lasts until the formation of a steady-state structure, which occurs within 5–9 ns after the end of the high-temperature stage.

Similar to the VACNT samples discussed in sections 3 and 4, the variation of the maximum initial inclination angle allows one to obtain CNT fibers with controllable structural characteristics. At small $\Theta_{max} = 3^\circ$ – 15° , the structure is dominated by relatively thick and almost straight bundles containing 15–50 CNTs with large columnar pores between them, Fig. 9a and b. The bundle thickness distributions are characterized by a broad maximum at 10–25 segments in a bundle cross section, Fig. 10a and b, and the average number of CNT segments in a bundle cross section, $\langle N_B \rangle$, equal to ~ 25 , Fig. 12. Qualitatively, the bundle size distributions generated at small inclination angles resemble those obtained for VACNT arrays FA and FB and shown in Fig. 5a and b. The values of HOF ≈ 0.85 (Fig. 12) and the average tilts of CNT segments, $\langle \theta \rangle = 14.0^\circ$ for $\Theta_{max} = 3^\circ$ and $\langle \theta \rangle = 13.2^\circ$ for $\Theta_{max} = 15^\circ$, are also very similar to the corresponding values listed for CNT forests FA and FB in Table 2. Thus, in the range of $\Theta_{max} \leq 15^\circ$, the procedure for generation of CNT networks developed in this work results in highly aligned CNT samples with a rather weak dependence of the structural parameters on the precise value of Θ_{max} .

With further increase in Θ_{max} above 15° , the structures of relaxed samples exhibit stronger dependence on Θ_{max} . An increasing Θ_{max} corresponds to the progressively increasing degree of entanglement of CNTs in the network structures, which is obvious from visual inspection of structures shown in Fig. 9c and d. Quantitatively, the increasing degree of entanglement is reflected in increasing average tortuosity $\langle \tau \rangle$ of nanotubes (Fig. 12), where the tortuosity of a CNT is defined as $\tau = L_{CNT}/C$, with C and L_{CNT} being the distance between two ends of the CNT and its length, respectively.

The formation of elongated, columnar pores in aligned fibers is in agreement with experimental observations, where the pore length (along the axis of the fiber) and the Porod chord length (characterizing the average lateral size of pores) obtained in synchrotron small-angle X-ray scattering (SAXS) measurements vary within ranges of 159–221 nm and 20.3–13.1 nm, respectively, with their ratio spanning the range from 7.8 to 16.9 [25]. The visual examination of the CNT fibers shown in Fig. 9a and b reveals that pores in these computational samples have lengths of ~ 300 – 400 nm and lateral sizes of ~ 100 nm, thus yielding the aspect ratios of ~ 3 – 4 . Less aligned samples, obtained at larger Θ_{max} and shown in Fig. 9c and d, have smaller pores with the pore lengths of ~ 200 – 300 nm and lateral sizes of ~ 30 – 50 nm, yielding the aspect ratios of ~ 6 – 10 . These structural parameters are comparable to those evaluated from the SAXS measurements, with somewhat smaller average pore sizes in experimental samples likely to be related to larger material densities of the experimental samples, which were not specified in Ref. [25].

At a sufficiently large Θ_{max} , e.g., $\Theta_{max} = 45^\circ$, there are a substantial number of CNT segments in the relaxed samples that are oriented perpendicular to the axis of the fiber, Fig. 11. In this case, the number of CNT segments in a bundle has a large peak at one and exhibits monotonous decrease with increasing number of CNTs segments in a bundle, Fig. 10d. Although such samples can include

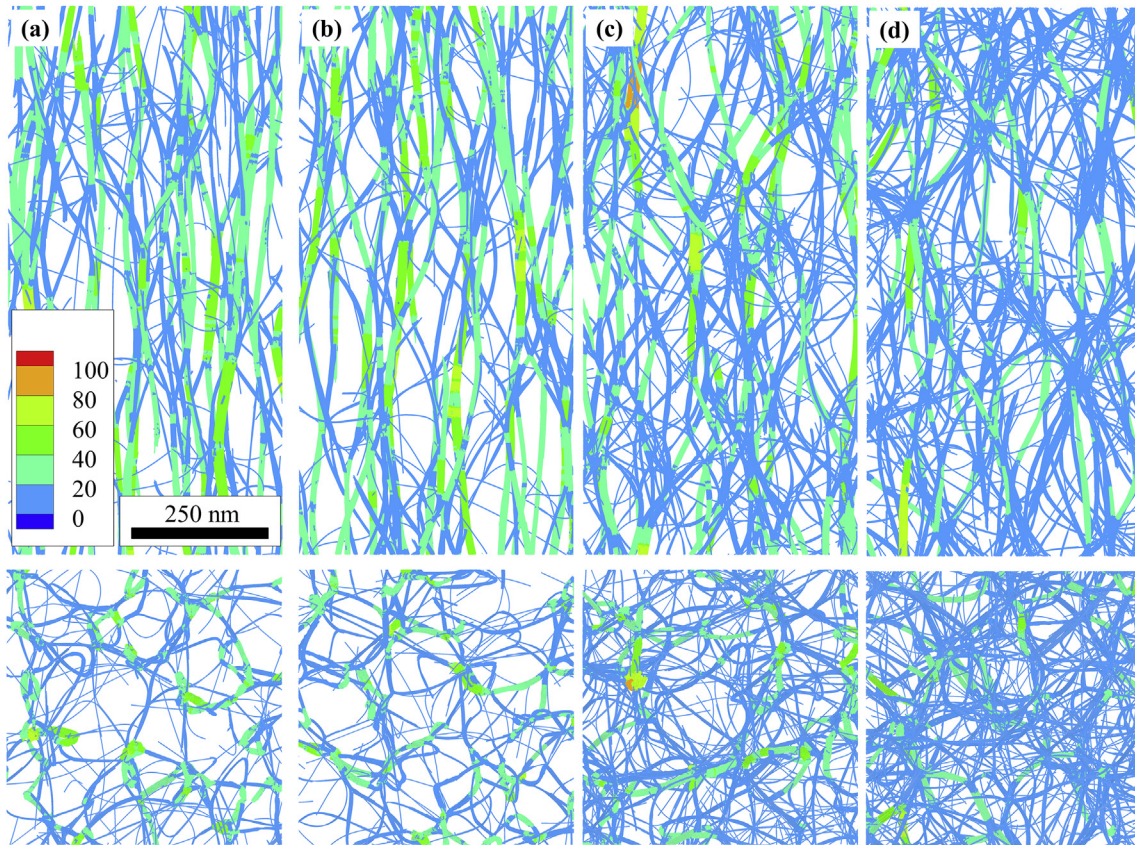


Fig. 9. Side and top views of relaxed samples of CNT fibers composed of 400-nm-long (10,10) CNTs obtained at maximum angles of initial inclination of CNTs Θ_{max} equal to 3° (a), 15° (b), 30° (c), and 45° (d). All samples have material density of 0.01 g/cm³ and dimensions of 1 × 1 × 1 μm³, although only the central parts of the samples with dimensions of 0.5 × 0.5 × 1 μm³ are shown in the figure. Individual nanotubes are colored according to the local thickness of bundles defined as the number of segments in a bundle cross section, with the scale shown in (a). The fiber axis is directed vertically in the top panels and normally to the plane of the figure in the bottom panels. (A colour version of this figure can be viewed online.)

bundles as thick as those in samples generated with $\Theta_{max} \leq 15^\circ$, the distribution demonstrates a strong depletion of bundles with more than 30 CNTs in a cross section and a corresponding decrease in the average bundle size from 25 at $\Theta_{max} \leq 15^\circ$ to 15 at $\Theta_{max} = 45^\circ$ (Fig. 12). The bundle size distributions for $\Theta_{max} = 30^\circ$ and $\Theta_{max} = 45^\circ$ (Fig. 10c and d) are quantitatively similar to that calculated for VACNT forest FC generated with $\Theta_{max} = 27^\circ$ and shown in Fig. 5c. Compared to the VACNT sample FC (Table 2), the fiber sample with $\Theta_{max} = 30^\circ$ has larger average bundle size $\langle N_B \rangle$ and smaller HOF, with the latter indicating a smaller degree of alignment of CNTs along the fiber axis. The larger $\langle N_B \rangle$ in the case of the fiber sample can be attributed to the additional freedom of individual CNTs that are not tethered to a substrate and are free to slide with respect to the surrounding nanotubes, as well as to the smaller density and increased duration of the high-temperature stage used in the generation of the fiber samples. Simulations performed for thin CNT films [47,49] demonstrated that all these factors favor an increase in the average bundle size in continuous CNT networks.

In Ref. [16], it was found that fibers composed of SWCNTs with diameters 1–2 nm consist of bundles of 10–30 nm in diameter. In order to translate the thickness of a bundle from the number of segments in a bundle cross section N_B given in Fig. 10 to the diameter D_B of an “equivalent” cylindrical bundle, one can assume close packing of CNTs in a bundle and equate the areas of the corresponding cross sections. With the distance between the CNT centers in the close packed hexagonal structure equal to $2R_T + \delta_e$,

where $R_T = 0.6785$ nm is the radius of (10,10) CNT and $\delta_e = 0.314$ nm is the equilibrium distance between the surfaces of nanotubes [47], we get $D_B = (2R_T + \delta_e)\sqrt{6N_B}/(\pi\sqrt{3}) = 1.67\sqrt{N_B}$ nm. For $N_B = 20$, which is a typical average bundle size $\langle N_B \rangle$ in the computational samples (Fig. 12), this equation yields $D_B \approx 7.5$ nm, while for $N_B = 50$, which corresponds to large bundles present in all generated fiber samples (Fig. 10), $D_B \approx 11.8$ nm. Thus, the bundles in the computational samples are at the lower end of the range reported for experimental samples in Ref. [16]. This can be explained by a substantially higher density of the experimental fibers, where the pore sizes are estimated to be in the range from ~1.5 to ~30 nm [16], i.e., much smaller than in the computational samples generated in this work.

In order to demonstrate the coarsening of bundles with increasing density of CNT fibers, a sample with density of 0.1 g/cm³, which is ten times higher than those discussed above, is generated with $\Theta_{max} = 15^\circ$ and illustrated in Fig. 13. Both the visual analysis of the sample configuration shown in Fig. 13a and the bundle size distribution in Fig. 13b indicate that the bundle thickness increases substantially with increasing material density. The maximum number of nanotubes in a bundle cross section is as large as 514, and the average bundle size $\langle N_B \rangle$ is equal to 109.6, which corresponds to the equivalent bundle diameter D_B of 17.5 nm. The latter value is in the middle of the range of 10–30 nm reported for the experimentally fabricated fibers in Ref. [16]. The strong sensitivity of the average bundle size to the material density provides further flexibility in tuning and optimizing the structural parameters of

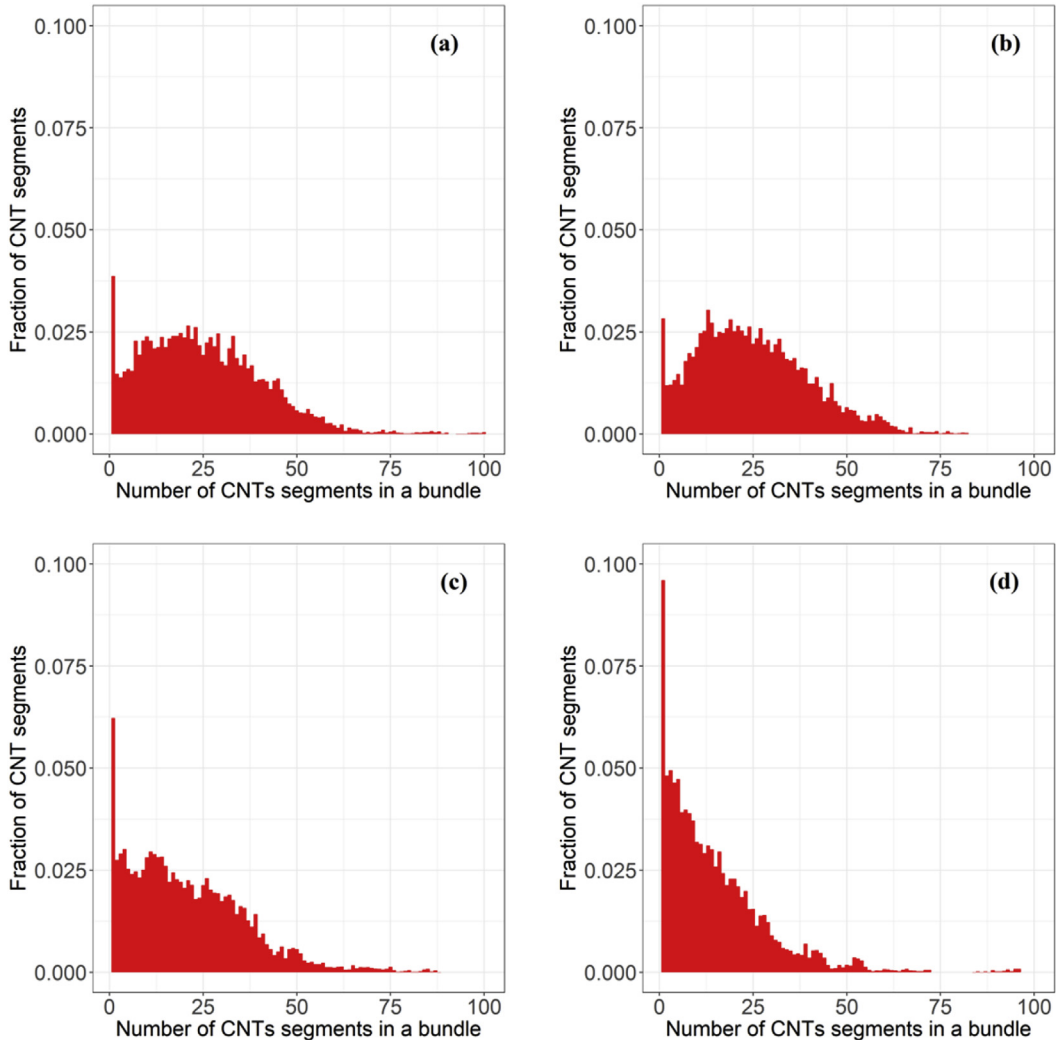


Fig. 10. The bundle thickness distributions calculated for computational samples of CNT fibers shown in Fig. 9 and obtained at maximum angles of initial inclination of CNTs Θ_{max} equal to 3° (a), 15° (b), 30° (c), and 45° (d). The bundle thickness is defined as the local number of CNTs present in a bundle cross section, and each bin covers a thickness increment by 1 CNT segment. (A colour version of this figure can be viewed online.)

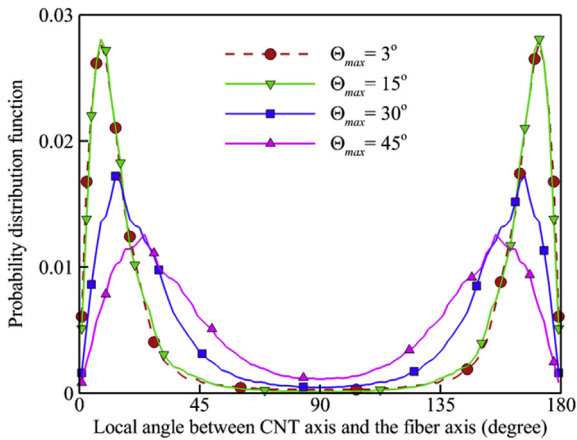


Fig. 11. Probability density function of the local angle between the CNT centerline and axis of the fiber calculated for computational samples of CNT fibers shown in Fig. 9 and obtained at maximum initial inclination angles of CNTs Θ_{max} equal to 3° (circles, red online), 15° (down-pointing triangles, green online), 30° (squares, blue online), and 45° (up-pointing triangles, magenta online). (A colour version of this figure can be viewed online.)

CNT fibers.

Similar to the observations from the structural characterization of CNT forests discussed in section 4, the network structures of CNT fibers exhibit almost linear dependence of the major structural parameters, including the HOF, average bundle size $\langle N_B \rangle$, and average tortuosity $\langle \tau \rangle$, on the maximum angle of initial inclination Θ_{max} , if Θ_{max} is larger than about 15° (Fig. 12). At $\Theta_{max} \leq 15^\circ$, the computational samples exhibit weak, if any, dependence of HOF, $\langle N_B \rangle$, and $\langle \tau \rangle$ on Θ_{max} . It is interesting to note that the decrease of HOF in the course of the relaxation of the initial samples composed of straight and dispersed CNTs (open diamonds in Fig. 12) is almost the same, 10–17%, for samples generated with different values of Θ_{max} . This observation and the linear relationships between the structural parameters and Θ_{max} at $\Theta_{max} \geq 15^\circ$ make it possible to pick an appropriate value of Θ_{max} in the sample generation procedure in order to obtain samples with desired values of HOF or $\langle N_B \rangle$. The relationship between $\langle N_B \rangle$ and HOF, however, is not unique and can be further adjusted by varying other parameters of the *in silico* sample preparation procedure, such as the duration and/or temperature of the high-temperature stage of the sample generation. By simultaneously varying several parameters of the sample preparation procedure, one can achieve fine control over

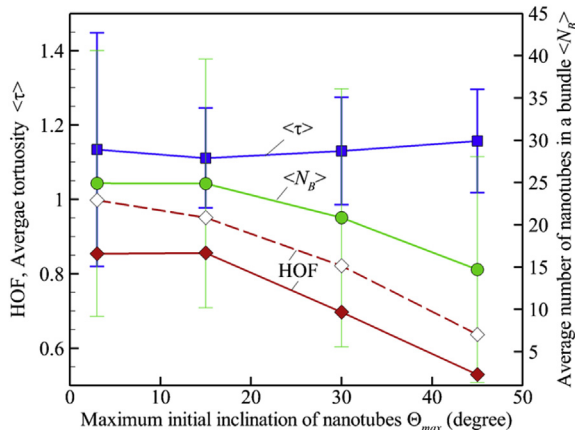


Fig. 12. Herman orientation factor HOF (diamonds), average bundle size $\langle N_B \rangle$ (circles), and average tortuosity of nanotubes $\langle \tau \rangle$ (squares) versus maximum angle of initial inclination of CNTs, Θ_{max} , used in the generation of CNT fibers composed of 400-nm-long (10,10) CNTs at material density of 0.01 g/cm^3 . Open diamonds with dashed curve correspond to HOF in the initial samples of straight and dispersed nanotubes; bold diamonds with solid curve correspond to HOF in the relaxed samples. Vertical error bars show the mean square deviation of the average tortuosity and bundle size. (A colour version of this figure can be viewed online.)

the degree of anisotropy characterized by the HOF and the degree of connectivity of nanotubes characterized by the averaged bundle size, to match those of a particular experimental sample.

7. Application of mesoscopic model to investigation of mechanical and thermal properties

The development of the sample preparation method capable of reproducing, for the first time, the experimentally observed mesoscopic structure of vertically aligned networks of nanotube bundles opens up a broad range of opportunities for investigation of mechanical and thermal transport properties of this important class of CNT materials. In this section, we only provide a few examples illustrating some of the potential applications of the dynamic mesoscopic model by preliminary results of first mesoscopic simulations performed for VACNT forests generated as discussed in section 3.

One broad area where the mesoscopic modeling can be highly instrumental is the analysis of the deformation mechanisms that control the mechanical properties of VACNT forests. The understanding of the mechanical properties is critical for a variety of applications, including energy absorption [87–89], electromechanical probing [90], fabrication of compliant contact structure for semiconductor packaging [91] and compression-modulated filter membranes [92]. One of the types of mechanical deformation that is commonly realized in the applications is the uniaxial compression of VACNT forests. The mechanical characteristics, including elastic modulus, yield stress, and resilience, characterizing uniaxial compression of VACNT forests reported in the literature are spanning several orders of magnitude [93–96]. Moreover, the recovery of uniaxially compressed VACNT forests also vary from near perfect [87,97] to mediocre [98,99]. The large variability of the mechanical properties is related to the high sensitivity of the structural

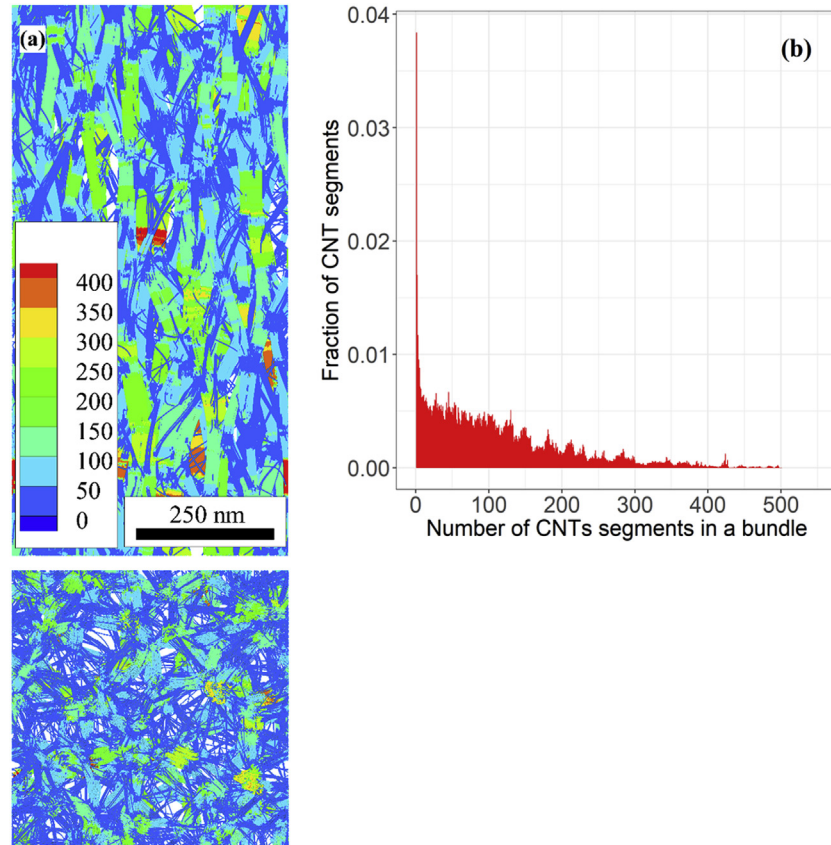


Fig. 13. Side and top views of a relaxed CNT fiber with material density of 0.1 g/cm^3 (a) and its bundle thickness distribution (b). The sample is composed of 400-nm-long (10,10) CNTs, has dimensions of $0.5 \times 0.5 \times 1 \mu\text{m}^3$, and is obtained with $\Theta_{max} = 15^\circ$. In panel (a), individual nanotubes are colored according to the local thickness of bundles they belong to. In both (a) and (b), the bundle thickness is defined as the local number of CNTs present in a bundle cross section. (A colour version of this figure can be viewed online.)

organization of these network materials to the growth methods and conditions [8,100], as well as to the presence of CNT defects [101,102] and contamination. Forest density and density gradients within a sample also influence the mechanical response during compression, and several works report linear dependence of the mechanical properties, such as the stiffness and elastic modulus, on density [102–104].

The relationship between the structural characteristics and mechanical properties of VACNT materials can be effectively and systematically explored in mesoscopic simulations performed for computational samples with realistic structures. This exploration is enabled by the computational procedure described in this paper and providing a high level of control over the structural characteristics of vertically aligned networks of nanotube bundles. A series of snapshots from a small-scale simulation of the uniaxial compression of a VACNT forest, shown in Fig. 14a–c, illustrates some of the capabilities of the mesoscopic modeling. The folding and bowing of the short CNT bundles in this simulation is facilitated by collective bending buckling of nanotubes in localized regions of bundles (red segments in the snapshots), which reduces the resistance of bundles to the bending deformation. The corresponding stress-strain curve predicted in the simulation (Fig. 14d) agrees well both qualitatively and quantitatively with stress responses measured in VACNT forest compression experiments [99]. In particular, three characteristic regimes, (i) elastic, (ii) plateau, and (iii) densification, commonly reported for VACNT forests [14,99,105], can be clearly identified in the simulated stress-strain curve shown in Fig. 14d. A thorough analysis of the uniaxial compression of *in-silico* VACNT forests is presented in a separate report [106].

The mesoscopic simulations can also be used for investigation of thermal transport properties of CNT networks, which hold promise

as thermal interface materials. Indeed, the values of the cooling rate reported for different CNT-based on-chip integrated cooling solutions for transporting and dissipation of heat from microelectronic devices are as high as 100 Wcm^{-2} [107] or even 5000 Wcm^{-2} [108], making CNT materials viable candidates for cooling systems of the next-generation microprocessors [108–113]. Moreover, the high degree of anisotropy of thermal conductivity of VACNT forests [114–116] opens up attractive opportunities for guiding the heat transport along a desired path in thermal management applications. In order to realize these opportunities, however, a clear understanding of the key microstructural features and elementary processes that control thermal transport properties of CNT network materials has to be achieved.

With the flexible approach to the generation of computational samples discussed in this paper, it is possible to perform a thorough investigation of the dependence of thermal conductivity on the structural characteristics of the anisotropic network structures. The values of thermal conductivity can be calculated by connecting the opposing sides of a CNT sample to two heat baths with different temperatures, obtaining the steady-state temperature profile along with the heat flux through the sample, and fitting the results to the Fourier law [50,60,66,68]. The values of the intrinsic thermal conductivity of CNTs and inter-tube conductance, needed for parametrization of the mesoscopic description of the heat transfer, can be obtained from results of experimental measurements, e.g., [117–120], or molecular dynamics simulations, e.g., [35–43,66].

The mesoscopic modeling of the heat transfer is illustrated in Fig. 15 for VACNT samples FA, FB, and FC discussed in sections 3 and 4. All CNT segments falling within 300 nm sections of either the top or base of the forest are assigned fixed temperatures, 300 and 600 K on the cold and hot sides, respectively, and the remaining nanotube segments are colored by the heat flux in the steady state regime. A

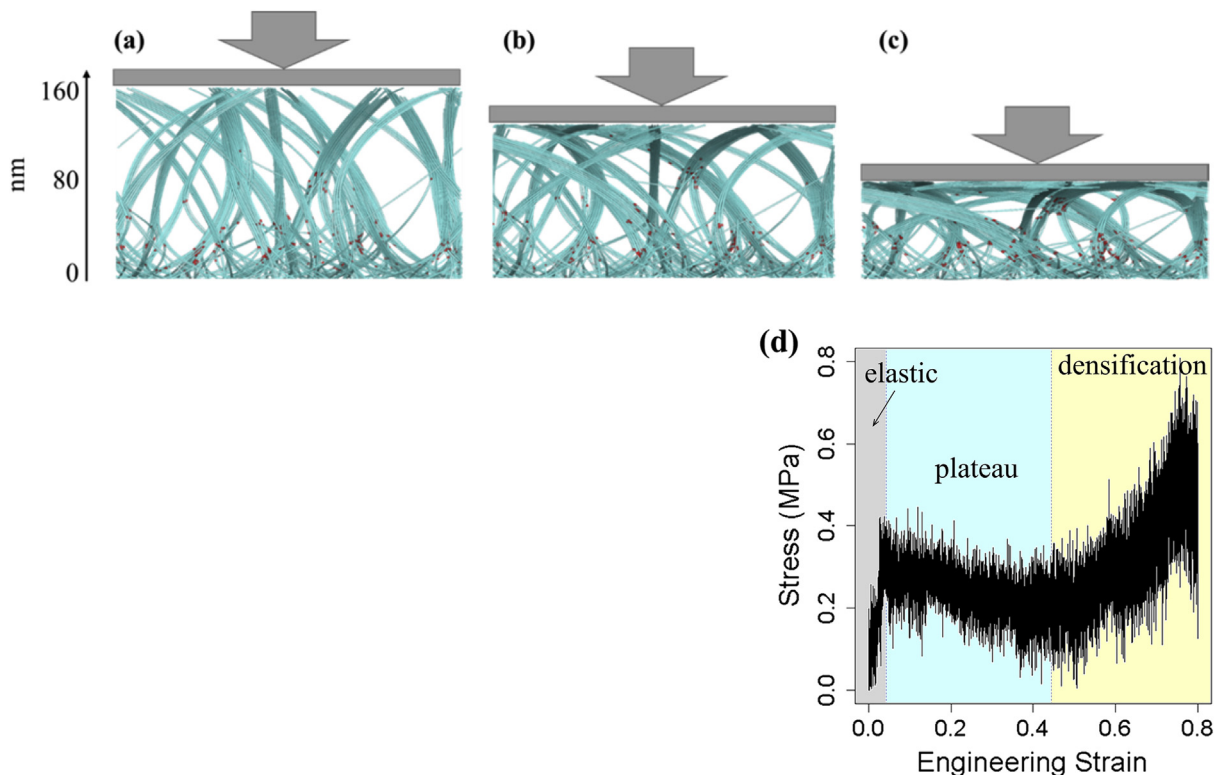


Fig. 14. A series of snapshots (a–c) and a stress-strain dependence (d) obtained in a mesoscopic simulation of uniaxial compression of the VACNT forest composed of 200-nm-long (10,10) CNTs prepared with $\Theta_{\max} = 27^\circ$ (see Fig. 8c). The snapshots are shown for compressive engineering strain of 0.2 (a), 0.4 (b) and 0.6 (c). The indenter velocity is 10 m/s, which corresponds to a deformation rate of $5 \times 10^7 \text{ s}^{-1}$. The CNT segments adjacent to the buckling kinks are colored red. (A colour version of this figure can be viewed online.)

visual inspection of the heat flux distributions suggests that the average heat flux is greatest in FA, and decreases for FB and FC samples. One can also discern that the heat flux is higher in the CNTs that belong to thick bundles crossing the sample from the hot to the cold heat bath regions, and is smaller for thin bundles and individual CNTs serving as interconnects between the thick bundles. This observation is in contrast to the results of the calculations performed for CNT films with random orientations of CNTs within the plane of the film [50,66,68], where the heat flux passing through the CNTs that are parts of the inter-bundle connections is found to be, on average, higher than in other parts of the network structures [66].

The predicted values of thermal conductivity of the VACNT samples are 17.6, 17.2, and 16.4 $\text{Wm}^{-1}\text{K}^{-1}$ for VACNT samples FA, FB, and FC, respectively. These computational predictions fall well within, the admittedly large, range of values measured for VACNT forests and fibers, e.g., 2.1 $\text{Wm}^{-1}\text{K}^{-1}$ [26,121], 42 $\text{Wm}^{-1}\text{K}^{-1}$ [115], and more than 200 $\text{Wm}^{-1}\text{K}^{-1}$ [114]. The corresponding effective conductivities recalculated on “per nanotube” basis are 1929, 1874, and 1771 $\text{Wm}^{-1}\text{K}^{-1}$ for the FA, FB, and FC samples, respectively. Given that the actual intrinsic conductivity of individual nanotubes is fixed at 2000 $\text{Wm}^{-1}\text{K}^{-1}$ in the calculations, the reduction of the effective conductivity is reflecting the “loss” of the conductivity due to the arrangement of CNTs into the continuous network. This reduction of the thermal conductivity exhibits a clear correlation with the decrease in the bundle size and the degree of CNT alignment, as can be seen from the structural characteristics of the three samples listed in Table 2.

Overall, the preliminary simulations performed for the VACNT forests reveal a significant sensitivity of the thermal conductivity to the structural details of the CNT networks and suggest that the conductivity can be controlled through the structural modification of VACNT materials with nominally identical macroscopic parameters, such as material density, type and length of the CNTs. Similar to CNT films [50], the thermal conductivity can be evaluated for different directions of the imposed heat flux, and the values of the conductivity can be related to the degree of anisotropy of the material structure. Moreover, the calculation of the thermal

conductivity for transient structures produced in the simulations of the mechanical loading, such as the ones shown in Fig. 14, can help to quantify the effect of the deformation on thermal transport and, in particular, reveal the changes in the conductivity upon critical events, such as the onset of collective buckling in CNT forests under compression or material failure under tension.

As a final example, out of many potential applications of the mesoscopic modeling of VACNT forests, we consider the CNT forest response to a high-velocity impact by a submicron projectile. The impact resistance of CNT materials is relevant to the exploration of the performance of these multifunctional low-density materials in aerospace applications [122,123] or as a protective armor [124], in the form of either pure CNT materials [125–127] or composites [128] reinforced with nanotubes. Using the mesoscopic model, we are in a position to methodically study the effect the CNT forest microstructure has on the absorption of the projectile energy. The development of the local heat bath approach, describing the energy redistribution between the collective degrees of freedom explicitly represented in the mesoscopic model and the internal degrees of freedom that correspond to the high-frequency atomic vibrations [67], enables a realistic representation of the energy dissipation in simulations of high-strain-rate deformation or impact loading, where the system can be expected to strongly deviate from the conditions of thermal equilibrium. As an illustration of this area of applications of mesoscopic modeling, a series of snapshots from a simulation of a platinum nanoparticle with diameter of 100 nm impacting the sample FB with an initial velocity of 100 m/s is shown in Fig. 16. Interestingly, a global deformation of the forest occurs despite the relatively small size of the nanoparticle. This suggests that the structural arrangement of nanotubes into the continuous network plays a key role in how the energy of the projectile is absorbed and redistributed.

Overall, the several examples briefly discussed above demonstrate that mesoscopic simulations performed for realistic computational samples generated with the method developed in this work are capable of capturing the complex interplay of an array of processes defining the mechanical behavior of CNT network materials under conditions of both quasi-static deformation and

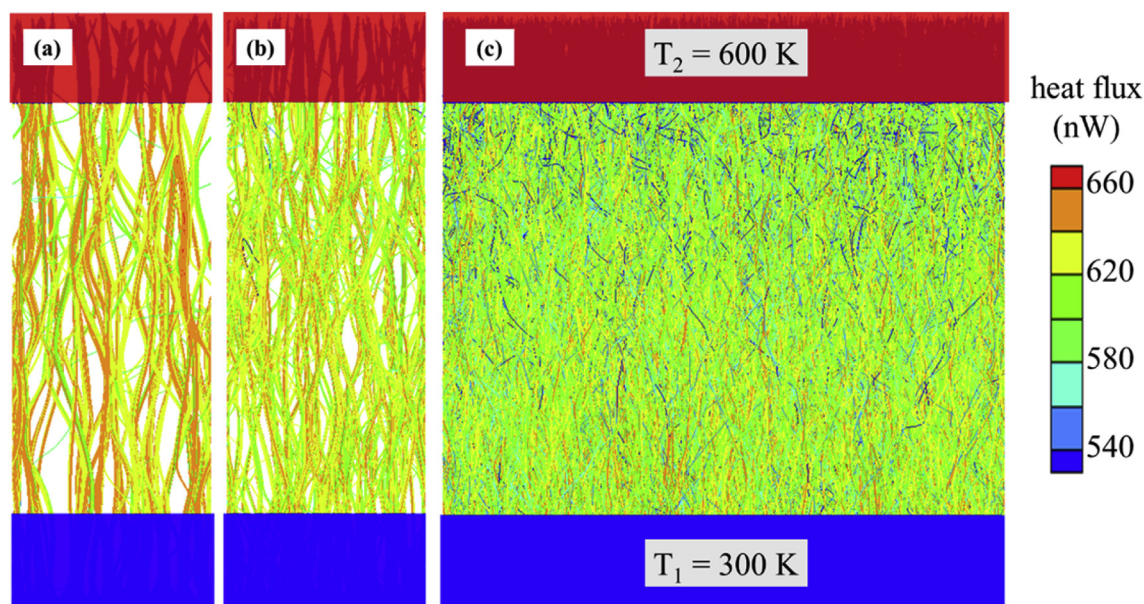


Fig. 15. The steady-state heat flux along the nanotubes obtained in the calculations of thermal conductivity of the VACNT samples FA (a), FB (b), and FC (c), see Table 1. The calculations are done assuming an intrinsic conductivity of 2000 $\text{W m}^{-1}\text{K}^{-1}$ for individual CNTs, and the inter-tube conductance is parametrized based on the results of atomistic simulations as explained in Refs. [43,50,60,66,68]. (A colour version of this figure can be viewed online.)

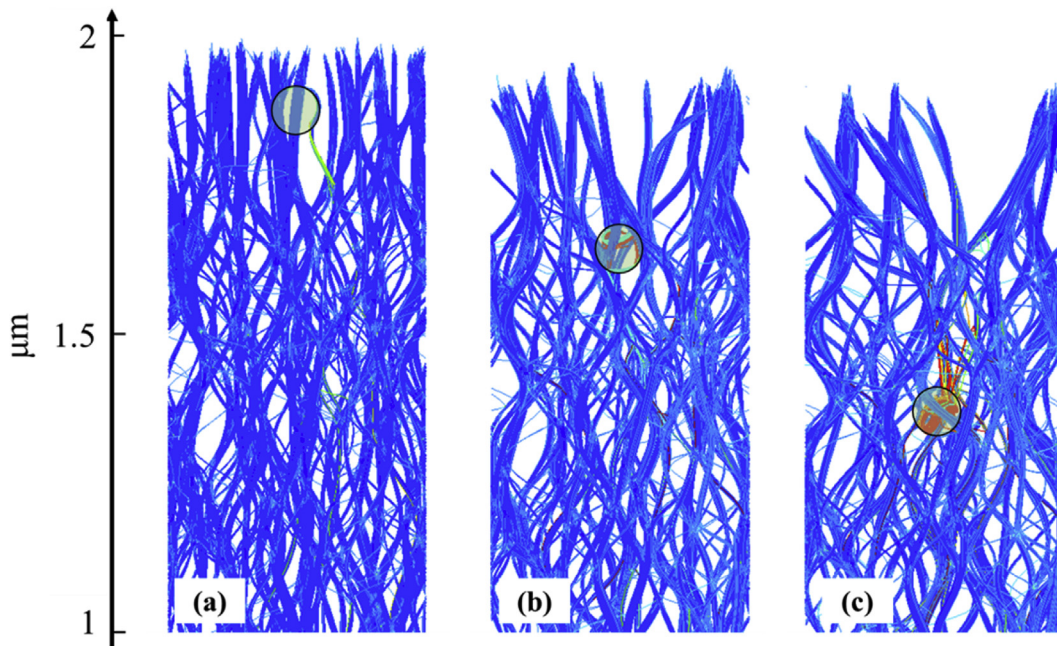


Fig. 16. Snapshots from a mesoscopic simulation of a high-velocity impact of a spherical Pt projectile with a diameter of 100 nm, a density of 21.45 g/cm^3 and an initial velocity of 100 m/s on the VACNT sample FB (see Table 1). The snapshots in (a), (b), and (c) are shown for 2.5 ns, 6.0 ns, and 10.0 ns after the impact, respectively. The nanotubes are colored by their local kinetic energy, and the location of the projectile is shown by a semitransparent circle drawn in front of the VACNT configuration. Note that although it appears that the projectile is exchanging energy with the CNTs only in its localized vicinity, the entire forest is deformed during the collision, as evidenced by the shrinking height of the sample. (A colour version of this figure can be viewed online.)

dynamic impact loading.

8. Summary

An effective and flexible method for *in silico* preparation of structurally distinct mesoscopic samples of vertically aligned networks of nanotube bundles is developed and applied to VACNT forests and CNT fibers. The method involves generation of an initial sample composed of straight nanotubes inclined with respect to the axis of the CNT forest/fiber, followed by a high-temperature annealing performed in a mesoscopic dynamic simulation and leading to structural self-organization of CNTs into an interconnected continuous network of CNT bundles.

The structures of the *in silico* generated VACNT forests and CNT fibers are characterized in terms of the bundle size distribution, average and maximum bundle sizes, the magnitude of the Herman orientation factor, the average tilt of CNT segments with respect to the direction of nanotube alignment in the forest/fiber structures, and the average tortuosity of the nanotubes. The structural parameters of the computational samples are compared with available experimental data and the ability of the developed computational procedure to produce structures closely matching those observed in experiments is demonstrated. Moreover, the structural parameters of the computational samples are found to exhibit a nearly linear dependence on the maximum angle of the initial inclination of nanotubes with respect to the direction of CNT alignment, thus providing an opportunity to precisely engineer the microstructure of computational samples to match those of particular experimental materials of interest.

The development of the sample preparation method capable of reproducing the experimentally observed mesoscopic structure of anisotropic networks of nanotube bundles opens up a broad range of opportunities for the computational exploration of structure – properties relationships in VACNT forests and CNT fibers. These opportunities are illustrated by first results obtained in mesoscopic

simulations of the uniaxial compression and nanoparticle impact resistance of VACNT forests, as well as the heat transfer through the aligned interconnected networks of bundles.

Acknowledgments

Financial support for this work is provided by the National Aeronautics and Space Administration (NASA) through an Early Stage Innovations grant from NASA's Space Technology Research Grants Program (NNX16AD99G). Computational support is provided by the National Science Foundation through the Extreme Science and Engineering Discovery Environment (Project CTS160026) and by NASA's Advanced Supercomputing (NAS) Division.

References

- [1] M.J. Schulz, V.N. Shanov, Z. Yin (Eds.), *Nanotube Superfiber Materials: Changing Engineering Design*, Elsevier, 2014.
- [2] A. Todri-Sanial, J. Dijon, A. Maffucci (Eds.), *Carbon Nanotubes for Interconnects: Process, Design and Applications*, Springer, 2017.
- [3] E.G. Rakov, Materials made of carbon nanotubes. The carbon nanotube forest, Russ. Chem. Rev. 82 (2013) 538–566.
- [4] M. Xu, D.N. Futaba, M. Yumura, K. Hata, Alignment control of carbon nanotube forest from random to nearly perfectly aligned by utilizing the crowding effect, ASC Nano 6 (2012) 5837–5844.
- [5] W. Cho, M. Schulz, V. Shanov, Growth and characterization of vertically aligned centimeter long CNT arrays, Carbon 72 (2014) 264–273.
- [6] M. Pinault, V. Pichot, H. Khodja, P. Launois, C. Reynaud, M. Mayne-L'Hermite, Evidence of sequential lift in growth of aligned multiwalled carbon nanotube multilayers, Nano Lett. 5 (2005) 2394–2398.
- [7] Q. Zhang, W. Zhou, W. Qian, R. Xiang, J. Huang, D. Wang, F. Wei, Synchronous growth of vertically aligned carbon nanotubes with pristine stress in the heterogeneous catalysis process, J. Phys. Chem. C 111 (2007) 14638–14643.
- [8] O. Yaglioglu, A. Cao, A.J. Hart, R. Martens, A.H. Slocum, Wide range control of microstructure and mechanical properties of carbon nanotube forests: a comparison between fixed and floating catalyst CVD techniques, Adv. Funct. Mat. 22 (2012) 5028–5037.
- [9] A.A. Puretzky, G. Eres, C.M. Rouleau, I.N. Ivanov, D.B. Geohegan, Real-time imaging of vertically aligned carbon nanotube array growth kinetics,

- Nanotechnology 19 (2008) 055605.
- [10] J.B. In, C.P. Grigoropoulos, A.A. Chernov, A. Noy, Growth kinetics of vertically aligned carbon nanotube arrays in clean oxygen-free conditions, *ACS Nano* 5 (2011) 9602–9610.
- [11] M.H. Rümmeli, C. Kramberger, F. Schäffel, E. Borowiak-Palen, T. Gemming, B. Rellinghaus, O. Jost, M. Löffler, P. Ayala, T. Pichler, R.J. Kalenczuk, Catalyst size dependencies for carbon nanotube synthesis, *Phys. Status Solidi B* 244 (2007) 3911–3915.
- [12] P.B. Amama, C.L. Pint, S.M. Kim, L. McJilton, K.G. Eyring, E.A. Stach, R.H. Hauge, B. Maruyama, Influence of alumina type on the evolution and activity of alumina-supported Fe catalysts in single-walled carbon nanotube carpet growth, *ACS Nano* 4 (2010) 895–904.
- [13] L. Zhu, D.W. Hess, C.-P. Wong, Monitoring carbon nanotube growth by formation of nanotube stacks and investigation of the diffusion-controlled kinetics, *J. Phys. Chem. B* 110 (2006) 5445–5449.
- [14] S. Pathak, E.J. Lim, P.P.S.S. Abadi, S. Graham, B.A. Cola, J.R. Greer, Higher recovery and better energy dissipation at faster strain rates in carbon nanotube bundles: An in-situ study, *ACS Nano* 6 (2012) 2189–2197.
- [15] P. Poulin, B. Vigolo, P. Launois, Films and fibers of oriented single wall nanotubes, *Carbon* 40 (2002) 1741–1749.
- [16] A.V. Neimark, S. Ruetsch, K.G. Kornev, P.I. Ravikovich, P. Poulin, S. Badaire, M. Maugey, Hierarchical pore structure and wetting properties of single-wall carbon nanotube fibers, *Nano Lett.* 3 (2003) 419–423.
- [17] X. Zhang, K. Jiang, C. Feng, P. Liu, L. Zhang, J. Kong, T. Zhang, Q. Li, S. Fan, Spinning and processing continuous yarn from 4-inch wafer scale super-aligned carbon nanotube arrays, *Adv. Mater.* 18 (2006) 1505–1510.
- [18] N. Behabtu, M.J. Green, M. Pasquali, Carbon nanotube-based neat fibers, *Nano Today* 3 (2008) 24–34.
- [19] N. Behabtu, C.C. Young, D.E. Tsentalovich, O. Kleinerman, X. Wang, A.W.K. Ma, E.A. Bengio, R.F. ter Waarbeek, J.J. de Jong, R.E. Hoogerwerf, S.B. Fairchild, J.B. Ferguson, B. Maruyama, J. Kono, Y. Talmon, Y. Cohen, M.J. Otto, M. Pasquali, Strong, light, multifunctional fibers of carbon nanotubes with ultrahigh conductivity, *Science* 339 (2013) 182–186.
- [20] D. Janas, K.K. Koziol, Carbon nanotube fibers and films: synthesis, applications and perspectives of the direct spinning method, *Nanoscale* 8 (2016) 19475–19490.
- [21] K. Koziol, J. Vilatela, A. Moisala, M. Motta, P. Cunniff, M. Sennett, A. Windle, High-performance carbon nanotube fiber, *Science* 318 (2007) 1892–1895.
- [22] K. Liu, Y. Sun, R. Zhou, H. Zhu, J. Wang, L. Liu, S. Fan, K. Jiang, Carbon nanotube yarns with high tensile strength made by a twisting and shrinking method, *Nanotechnology* 21 (2010) 045708.
- [23] R. Downes, S. Wang, D. Haldane, A. Moench, R. Liang, Strain-induced alignment mechanisms of carbon nanotube networks, *Adv. Eng. Mater.* 17 (2015) 349–358.
- [24] R.D. Downes, A. Hao, J.G. Park, Y.-F. Su, R. Liang, B.D. Jensen, E.J. Siochi, K.E. Wise, Geometrically constrained self-assemble and crystal packing of flattened and aligned carbon nanotubes, *Carbon* 93 (2015) 953–966.
- [25] H. Yue, V. Reguero, E. Senokos, A. Monreal-Bernal, B. Mas, J.P. Fernández-Blázquez, R. Marcilla, J.J. Vilatela, Fractal carbon nanotube fibers with mesoporous crystalline structure, *Carbon* 122 (2017) 47–53.
- [26] G. Chen, D.N. Futaba, H. Kimura, S. Sakurai, M. Yumura, K. Hata, Absence of an ideal single-walled carbon nanotube forest structure for thermal and electrical conductivities, *ACS Nano* 7 (2013) 10218–10224.
- [27] M.P. Allen, D.J. Tildesley, *Computer Simulation of Liquids*, Oxford Science Publications, 1987.
- [28] B.I. Yakobson, C.J. Brabec, J. Bernholc, Nanomechanics of carbon tubes: instabilities beyond linear response, *Phys. Rev. Lett.* 76 (1996) 2511–2514.
- [29] S. Iijima, C. Brabec, A. Maiti, J. Bernholc, Structural flexibility of carbon nanotubes, *J. Chem. Phys.* 104 (1996) 2089–2092.
- [30] T. Xiao, K. Liao, Nonlinear elastic properties of carbon nanotubes subjected to large axial deformations, *Phys. Rev. B* 66 (2002) 153407.
- [31] T. Belytschko, S.P. Xiao, G.C. Schatz, R.S. Ruoff, Atomistic simulations of nanotube fracture, *Phys. Rev. B* 65 (2002) 235430.
- [32] S.L. Mielke, D. Troya, S. Zhang, J.-L. Li, S. Xiao, R. Car, R.S. Ruoff, G.C. Schatz, T. Belytschko, The role of vacancy defects and holes in the fracture of carbon nanotubes, *Chem. Phys. Lett.* 390 (2004) 413–420.
- [33] K.M. Liew, X.Q. He, C.H. Wong, On the study of elastic and plastic properties of multi-walled carbon nanotubes under axial tension using molecular dynamics simulation, *Acta Mater.* 52 (2004) 2521–2527.
- [34] C.M. Wang, Y.Y. Zhang, Y. Xiang, J.N. Reddy, Recent studies on buckling of carbon nanotubes, *Appl. Mech. Rev.* 63 (2010) 030804.
- [35] J. Park, M.F. Bifano, V. Prakash, Sensitivity of thermal conductivity of carbon nanotubes to defect concentration and heat-treatment, *J. Appl. Phys.* 113 (2013), 034312.
- [36] S. Berber, Y.-K. Kwon, D. Tomanek, Unusually high thermal conductivity of carbon nanotubes, *Phys. Rev. Lett.* 84 (2000) 4613–4616.
- [37] R.N. Salaway, L.V. Zhigilei, Molecular dynamics simulations of thermal conductivity of carbon nanotube: Resolving the effects of computational parameters, *Int. J. Heat Mass Tran.* 70 (2014) 954–964.
- [38] Z. Xu, M.J. Buehler, Strain controlled thermomutability of single-walled carbon nanotubes, *Nanotechnology* 20 (2009) 185701.
- [39] C. Ren, W. Zhang, Z. Xu, Z. Zhu, P. Huai, Thermal conductivity of single-walled carbon nanotubes under axial stress, *J. Phys. Chem. C* 114 (2010) 5786–5791.
- [40] W.J. Evans, M. Shen, P. Kebinski, Inter-tube thermal conductance in carbon nanotubes arrays and bundles: effects of contact area and pressure, *Appl. Phys. Lett.* 100 (2012) 261908.
- [41] A.N. Volkov, R.N. Salaway, L.V. Zhigilei, Atomistic simulations, mesoscopic modeling, and theoretical analysis of thermal conductivity of bundles composed of carbon nanotubes, *J. Appl. Phys.* 114 (2013) 104301.
- [42] L. Hu, A.J.H. McGaughey, Thermal conductance of the junction between single-walled carbon nanotubes, *Appl. Phys. Lett.* 105 (2014) 193104.
- [43] R.N. Salaway, L.V. Zhigilei, Thermal conductance of carbon nanotube contacts: Molecular dynamics simulations and general description of the contact conductance, *Phys. Rev. B* 94 (2016) 014308.
- [44] M. Buehler, Mesoscale modeling of mechanics of carbon nanotubes: self-assembly, self-folding, and fracture, *J. Mater. Res.* 21 (2006) 2855–2869.
- [45] I. Ostanin, R. Ballarini, D. Potyondy, T. Dumitriță, A distinct element method for large scale simulations of carbon nanotube assemblies, *J. Mech. Phys. Solid.* 61 (2013) 762–782.
- [46] L.V. Zhigilei, C. Wei, D. Srivastava, Mesoscopic model for dynamic simulations of carbon nanotubes, *Phys. Rev. B* 71 (2005) 165417.
- [47] A.N. Volkov, L.V. Zhigilei, Mesoscopic interaction potential for carbon nanotubes of arbitrary length and orientation, *J. Phys. Chem. C* 114 (2010) 5513–5531.
- [48] S.W. Cranford, M.J. Buehler, *In silico* assembly and nanomechanical characterization of carbon nanotube buckypaper, *Nanotechnology* 21 (2010) 265706.
- [49] A.N. Volkov, L.V. Zhigilei, Structural stability of carbon nanotube films: The role of bending buckling, *ACS Nano* 4 (2010) 6187–6195.
- [50] A.N. Volkov, L.V. Zhigilei, Scaling laws and mesoscopic modeling of thermal conductivity in carbon nanotube materials, *Phys. Rev. Lett.* 104 (2010) 215902.
- [51] E.A. Colbourn (Ed.), *Computer Simulation of Polymers*, Longman, Harlow, 1994.
- [52] B. Xie, Y. Liu, Y. Ding, Q. Zheng, Z. Xu, Mechanics of carbon nanotube networks: microstructural evolution and optimal design, *Soft Matter* 7 (2011) 10039–10047.
- [53] C. Wang, B. Xie, Y. Liu, Z. Xu, Mechanotunable microstructures of carbon nanotube networks, *ACS Macro Lett.* 1 (2012) 1176–1179.
- [54] Y. Li, M. Kröger, Viscoelasticity of carbon nanotube buckypaper: zipping-unzipping mechanism and entanglement effects, *Soft Matter* 8 (2012) 7822–7830.
- [55] Y. Li, M. Kröger, A theoretical evaluation of the effects of carbon nanotube entanglement and bundling on the structural and mechanical properties of buckypaper, *Carbon* 50 (2012) 1793–1806.
- [56] Y. Li, M. Kröger, Computational study on entanglement length and pore size of carbon nanotube buckypaper, *Appl. Phys. Lett.* 100 (2012) 021907.
- [57] M.G. Hahn, H. Wang, H.Y. Jung, S. Hong, S.-G. Lee, S.-R. Kim, M. Upmanyu, Y.J. Jung, Bundling dynamics regulates the active mechanics and transport in carbon nanotube networks and their nanocomposites, *Nanoscale* 4 (2012) 3584–3590.
- [58] J. Zhao, J.-W. Jiang, L. Wang, W. Guo, T. Rabczuk, Coarse-grained potentials of single-walled carbon nanotubes, *J. Mech. Phys. Solid.* 71 (2014) 197–218.
- [59] Y. Won, Y. Gao, M.A. Panzer, R. Xiang, S. Maruyama, T.W. Kenny, W. Cai, K.E. Goodson, Zipping, entanglement, and the elastic modulus of aligned single-walled carbon nanotube films, *PNAS* 110 (2013) 20426–20430.
- [60] L.V. Zhigilei, R.N. Salaway, B.K. Wittmaack, A.N. Volkov, Computational studies of thermal transport properties of carbon nanotube materials, in: A. Todri-Sanial, J. Dijon, A. Maffucci (Eds.), *Carbon Nanotubes for Interconnects: Process, Design and Applications*, Springer, 2017, pp. 129–161.
- [61] M.R. Maschmann, Integrated simulation of active CNT forest growth and mechanical compression, *Carbon* 86 (2015) 26–37.
- [62] Y. Wang, C. Gaidău, I. Ostanin, T. Dumitriță, Ring windings from single-wall carbon nanotubes: a distinct element method study, *Appl. Phys. Lett.* 103 (2013) 183902.
- [63] I. Ostanin, R. Ballarini, T. Dumitriță, Distinct element method modeling of carbon nanotube bundles with intertube sliding and dissipation, *J. Appl. Mech.* 81 (2014) 061004.
- [64] P.A. Cundall, O. Strack, A discrete numerical model for granular assemblies, *Geotechnique* 29 (1979) 47–65.
- [65] P.A. Cundall, Formulation of a three-dimensional distinct element model - Part I: A scheme to detect and represent contacts in a system composed of many polyhedral blocks, *Int. J. Rock Mech. Min. Sci. Geomech. Abstr.* 25 (1988) 107–116.
- [66] A.N. Volkov, T. Shiga, D. Nicholson, J. Shiomi, L.V. Zhigilei, Effect of bending buckling of carbon nanotubes on thermal conductivity of carbon nanotube materials, *J. Appl. Phys.* 111 (2012) 053501.
- [67] W.M. Jacobs, D.A. Nicholson, H. Zemer, A.N. Volkov, L.V. Zhigilei, Acoustic energy dissipation and thermalization in carbon nanotubes: Atomistic modeling and mesoscopic description, *Phys. Rev. B* 86 (2012) 165414.
- [68] A.N. Volkov, L.V. Zhigilei, Heat conduction in carbon nanotube materials: Strong effect of intrinsic thermal conductivity of carbon nanotubes, *Appl. Phys. Lett.* 101 (2012) 043113.
- [69] D.W. Brenner, Empirical potential for hydrocarbons for use in simulating the chemical vapor deposition of diamond films, *Phys. Rev. B* 42 (1990) 9458–9471.
- [70] D.W. Brenner, O.A. Shenderova, J.A. Harrison, S.J. Stuart, B. Ni, S.B. Sinnott, A second-generation reactive empirical bond order (REBO) potential energy expression for hydrocarbons, *J. Phys. Condens. Matter* 14 (2002) 783–802.

- [71] S.J. Stuart, A.B. Tutein, J.A. Harrison, A reactive potential for hydrocarbons with intermolecular interactions, *J. Chem. Phys.* 112 (2000) 6472–6486.
- [72] B. Bhushan, Nanotribology of carbon nanotubes, *J. Phys.: Condens. Matter* 20 (2008) 365214.
- [73] O. Suekane, A. Nagataki, H. Mori, Y. Nakayama, Static friction force of carbon nanotube surfaces, *Appl. Phys. Express* 1 (2008) 064001.
- [74] G.F. Zhong, T. Iwasaki, H. Kawarada, Semi-quantitative study on the fabrication of densely-packed and vertically aligned single-walled carbon nanotubes, *Carbon* 44 (2006) 2009–2014.
- [75] D.N. Futaba, K. Hata, T. Yamada, T. Hiraoka, Y. Hayamizu, Y. Kakudate, O. Tanaike, H. Hatori, M. Yumura, S. Iijima, Shape-engineerable and highly densely packed single-walled carbon nanotubes and their application as super-capacitor electrodes, *Nat. Mater.* 5 (2006) 987–994.
- [76] S.L. Kang, C. Kocabas, T. Ozel, M. Shim, N. Pimparkar, M.A. Alam, S.V. Rotkin, J.A. Rogers, High performance electronics using dense, perfectly aligned arrays of single walled carbon nanotubes, *Nat. Mater.* 2 (2007) 230–236.
- [77] E. Einarrson, H. Shiozawa, C. Kramberger, M.H. Rümmeli, A. Grüneis, T. Pichler, S. Maruyama, Revealing the small-bundle internal structure of vertically aligned single-walled carbon nanotube films, *J. Phys. Chem. C* 111 (2007) 17861–17864.
- [78] G. Zhong, J.H. Warner, M. Fouquet, A.W. Robertson, B. Chen, J. Robertson, Growth of ultrahigh density single-walled carbon nanotube forests by improved catalyst design, *ACS Nano* 6 (2012) 2893–2903.
- [79] G. Chen, Y. Seki, H. Kimura, S. Sakurai, M. Yumura, K. Hata, D.N. Futaba, Diameter control of single-walled carbon nanotube forests from 1.3–3.0 nm by arc plasma deposition, *Sci. Rep.* 4 (2014) 3804.
- [80] A.N. Volkov, K.R. Simov, L.V. Zhigilei, Mesoscopic simulation of self-assembly of carbon nanotubes into a network of bundles, in: Proceedings of the 47th AIAA Aerospace Sciences Meeting, 2009, AIAA paper 2009-1544.
- [81] Data Files Defining the Structures of VACNT Computational Samples FA, FB, FC, and FD are accessible from <http://www.faculty.virginia.edu/CompMat/VACNT-samples/>.
- [82] H.J.C. Berendsen, J.P.M. Postma, W.F. van Gunsteren, A. DiNola, J.R. Haak, Molecular dynamics with coupling to an external bath, *J. Chem. Phys.* 81 (1984) 3684–3690.
- [83] J. Yang, S. Esconjauregui, A.W. Robertson, Y. Guo, T. Hallam, H. Sugime, G. Zhong, G.S. Duesberg, J. Robertson, Growth of high-density carbon nanotube forests on conductive TiSiN supports, *Appl. Phys. Lett.* 106 (2015) 083108.
- [84] G. Zhong, J. Yang, H. Sugime, R. Rao, J. Zhao, D. Liu, A. Harutyunyan, J. Robertson, Growth of high quality, high density single-walled carbon nanotube forests on copper foils, *Carbon* 98 (2016) 624–632.
- [85] C. Kramberger, T. Thurakitseree, H. Shiozawa, A. Stangl, Y. Izumi, T. Kinoshita, T. Muro, T. Pichler, S. Maruyama, Length scales in orientational order of vertically aligned single walled carbon nanotubes, *Phys. Status Solidi B* 250 (2013) 2631–2634.
- [86] W. Deng, X. Chen, X. Chen, Z. Liu, Y. Zheng, A. Hu, Y. Xiong, Z. Li, Q. Tang, Alignment and structural control of nitrogen-doped carbon nanotubes by utilizing precursor concentration effect, *Nanotechnology* 25 (2014) 475601.
- [87] A. Cao, P.L. Dickrell, W.G. Sawyer, M.N. Ghasemi-Nejhad, P.M. Ajayan, Super-compressible foamlike carbon nanotube films, *Science* 310 (2005) 1307–1310.
- [88] Y. Gogotsi, High-temperature rubber made from carbon nanotubes, *Science* 330 (2010) 1332–1333.
- [89] A. Misra, J.R. Greer, C. Daraio, Strain rate effects in the mechanical response of polymer-anchored carbon nanotube foams, *Adv. Mater.* 21 (2009) 334–338.
- [90] O. Yaglioglu, R. Martens, A.J. Hart, A.H. Slocum, Conductive carbon nanotube composite micropores, *Adv. Mater.* 20 (2008) 357–362.
- [91] O. Yaglioglu, R. Martens, A. Cao, A.H. Slocum, Compliant carbon nanotube–metal contact structures, in: Proc. 57th IEEE Holm Conf. Electrical Contacts, 2011, Minneapolis, USA.
- [92] X. Li, G. Zhu, J.S. Dordick, P.M. Ajayan, Compression-modulated tunable-pore carbon-nanotube membrane filters, *Small* 3 (2007) 595–599.
- [93] J. Suhr, P. Victor, L. Ci, S. Sreekala, X. Zhang, O. Nalamasu, P.M. Ajayan, Fatigue resistance of aligned carbon nanotube arrays under cyclic compression, *Nat. Nanotechnol.* 2 (2007) 417–421.
- [94] T. Tong, Y. Zhao, L. Delzeit, A. Kashani, M. Meyyappan, A. Majumdar, Height independent compressive modulus of vertically aligned carbon nanotube arrays, *Nano Lett.* 8 (2008) 511–515.
- [95] P.D. Bradford, X. Wang, H. Zhao, Y.T. Zhu, Tuning the compressive mechanical properties of carbon nanotube foam, *Carbon* 49 (2011) 2834–2841.
- [96] C.P. Deck, J. Flowers, G.S.B. McKee, K. Vecchio, Mechanical behavior of ultralong multiwalled carbon nanotube mats, *J. Appl. Phys.* 101 (2007) 023512.
- [97] M. Xu, D.N. Futaba, T. Yamada, M. Yumura, K. Hata, Carbon nanotubes with temperature-invariant viscoelasticity from −196° to 1000°C, *Science* 330 (2010) 1364–1368.
- [98] Q. Zhang, Y.C. Lu, F. Du, L. Dai, J. Baur, D.C. Foster, Viscoelastic creep of vertically aligned carbon nanotubes, *J. Phys. D: Appl. Phys.* 43 (2010) 315401.
- [99] S.B. Hutchens, L.J. Hall, J.R. Greer, In situ mechanical testing reveals periodic buckle nucleation and propagation in carbon nanotube bundles, *Adv. Funct. Mater.* 20 (2010) 2338–2346.
- [100] M. Kumar, Y. Ando, Chemical vapor deposition of carbon nanotubes: a review on growth mechanism and mass production, *J. Nanosci. Nanotechnol.* 10 (2010) 3739–3758.
- [101] E.F. Antunes, A.O. Lobo, E.J. Corat, V.J. Trava-Airoldi, A.A. Martin, C. Veríssimo, Comparative study of first- and second-order Raman spectra of MWCNT at visible and infrared laser excitation, *Carbon* 44 (2006) 2202–2211.
- [102] E.F. Antunes, A.O. Lobo, E.J. Corat, V.J. Trava-Airoldi, Influence of diameter in the Raman spectra of aligned multi-walled carbon nanotubes, *Carbon* 45 (2007) 913–921.
- [103] S. Pathak, N. Mohan, E. Decovenraere, A. Needleman, M. Bedewy, A.J. Hart, J.R. Greer, Local relative density modulates failure and strength in vertically aligned carbon nanotubes, *ACS Nano* 7 (2013) 8593–8604.
- [104] Y. Li, J. Kang, J. Choi, J. Nam, J. Suhr, Determination of material constants of vertically aligned carbon nanotube structures in compressions, *Nanotechnology* 26 (2015) 245701.
- [105] A.A. Zbib, S. Dj Mesarovic, E.T. Lilleodden, D. McClain, J. Jiao, D.F. Bahr, The coordinated buckling of carbon nanotube turfs under uniform compression, *Nanotechnology* 19 (2008) 175704.
- [106] B.K. Wittmaack, A.N. Volkov, L.V. Zhigilei, Mesoscopic modeling of the uniaxial compression and recovery of vertically aligned carbon nanotube forests, *Compos. Sci. Technol.* (2018) submitted.
- [107] K. Kordás, G. Tóth, P. Moilanen, M. Kumpumäki, J. Vähäkangas, A. Uusimäki, R. Vajtai, P.M. Ajayan, Chip cooling with integrated carbon nanotube microfin architectures, *Appl. Phys. Lett.* 90 (2007) 123105.
- [108] Y. Fu, N. Nabiollahi, T. Wang, S. Wang, Z. Hu, B. Carlberg, Y. Zhang, X. Wang, J. Liu, A complete carbon-nanotube-based on-chip cooling solution with very high heat dissipation capacity, *Nanotechnology* 23 (2012) 045304.
- [109] H. Huang, C. Liu, Y. Wu, S. Fan, Aligned carbon nanotube composite films for thermal management, *Adv. Mater.* 17 (2005) 1652–1656.
- [110] X. Liu, Y. Zhang, A.M. Cassell, B.A. Cruden, Implications of catalyst control for carbon nanotube based thermal interface materials, *J. Appl. Phys.* 104 (2008) 084310.
- [111] P.E. Lyons, S. De, F. Blighe, V. Nicolosi, L.F.C. Pereira, M.S. Ferreira, J.N. Coleman, The relationship between network morphology and conductivity in nanotube films, *J. Appl. Phys.* 104 (2008) 044302.
- [112] M. Akoshima, K. Hata, D.N. Futaba, K. Mizuno, T. Baba, M. Yumura, Thermal diffusivity of single-walled carbon nanotube forest measured by laser flash method, *Jpn. J. Appl. Phys.* 48 (2009) 05EC07.
- [113] S. Kaur, N. Raravikar, B.A. Helms, R. Prasher, D.F. Ogletree, Enhanced thermal transport at covalently functionalized carbon nanotube array interfaces, *Nat. Comm.* 5 (2014) 3082.
- [114] J. Hone, M.C. Laguno, N.M. Nemes, A.T. Johnson, J.E. Fischer, D.A. Walters, M.J. Casavant, J. Schmidt, R.E. Smalley, Electrical and thermal transport properties of magnetically aligned single wall carbon nanotube films, *Appl. Phys. Lett.* 77 (2000) 666–668.
- [115] P. Gonnet, S.Y. Liang, E.S. Choi, R.S. Kadambala, C. Zhang, J.S. Brooks, B. Wang, L. Kramer, Thermal conductivity of magnetically aligned carbon nanotube buckypapers and nanocomposites, *Curr. Appl. Phys.* 6 (2006) 119–122.
- [116] I. Ivanov, A. Puretzky, G. Eres, H. Wang, Z. Pan, H. Cui, R. Jin, J. Howe, D.B. Geohegan, Fast and highly anisotropic thermal transport through vertically aligned carbon nanotube arrays, *Appl. Phys. Lett.* 89 (2006) 223110.
- [117] M. Fujii, X. Zhang, H. Xie, H. Ago, K. Takahashi, T. Ikuta, H. Abe, T. Shimizu, Measuring the thermal conductivity of a single carbon nanotube, *Phys. Rev. Lett.* 95 (2005) 065502.
- [118] Q. Li, C. Liu, X. Wang, S. Fan, Measuring the thermal conductivity of individual carbon nanotubes by the Raman shift method, *Nanotechnology* 20 (2009) 145702.
- [119] A.A. Balandin, Thermal properties of graphene and nanostructured carbon materials, *Nat. Mater.* 10 (2011) 569–581.
- [120] J. Yang, S. Waltermire, Y. Chen, A.A. Zinn, T.T. Xu, D. Li, Contact thermal resistance between individual multiwall carbon nanotubes, *Appl. Phys. Lett.* 96 (2010) 023109.
- [121] T. Ji, Y. Feng, M. Qin, W. Feng, Thermal conducting properties of aligned carbon nanotubes and their polymer composites, *Composites: Part A* 91 (2016) 351–369.
- [122] J. Baur, E. Silverman, Challenges and opportunities in multifunctional nanocomposite structures for aerospace applications, *MRS Bull.* 32 (2007) 328–334.
- [123] T. Ishikawa, Overview of trends in advanced composite research and applications in Japan, *Adv. Comp. Mater.* 15 (2006) 3–37.
- [124] R. Yadav, M. Naebe, X. Wang, B. Kandasubramanian, Body armour materials: from steel to contemporary biomimetic systems, *RCS Adv.* 6 (2016) 115145–115174.
- [125] K. Mylvaganam, L.C. Zhang, Energy absorption capacity of carbon nanotubes under ballistic impact, *Appl. Phys. Lett.* 89 (2006) 123127.
- [126] K. Mylvaganam, L.C. Zhang, Ballistic resistance capacity of carbon nanotubes, *Nanotechnology* 18 (2007) 475701.
- [127] C. Daraio, V.F. Nesterenko, S. Jin, Impact response by a foamlike forest of coiled carbon nanotubes, *J. Appl. Phys.* 100 (2006) 064309.
- [128] L. Sun, R.F. Gibson, F. Gordaninejad, J. Suhr, Energy absorption capability of nanocomposite: a review, *Compos. Sci. Technol.* 69 (2009) 2329–2409.